AD-A069 965 CALIFORNIA UNIV LOS ANGELES DEPT OF MATERIALS F/G 11/6
ACOUSTIC EMISSION BEHAVIOUR OF A LOW ALLOY STEEL.(U)
MAY 79 R J LANDY N00014-75-C-0419
UNCLASSIFIED TR-79-02 NL

1 OF 2
AD A069965

LEVEL II

(10)

Technical Report No. 79-02
to the
Office of Naval Research
Contract No. N00014-75-C-0419
(15)

AD A069965

(6) ACOUSTIC EMISSION BEHAVIOUR OF A LOW ALLOY STEEL.

(9) Master's thesis,

by

(10) Robert James/Landy

Materials Department
School of Engineering and Applied Science
University of California
Los Angeles, California 90024

DDC
RECEIVED
JUN 13 1979
C

(14) TR-79-02

(11) May 1979

(12) 113p.

Reproduction whole or in part is permitted for any purpose of the United States Government.

DDC FILE COPY

This document has been approved for public release and sale; its distribution is unlimited.

79 06 12 154

406 237 LB

SECURITY CLASSIFICATION OF THIS PAGE (When Data Entered)

REPORT DOCUMENTATION PAGE		READ INSTRUCTIONS BEFORE COMPLETING FORM
1. REPORT NUMBER ONR Technical Report No. 79-02	2. GOVT ACCESSION NO.	3. RECIPIENT'S CATALOG NUMBER
4. TITLE (and Subtitle) Acoustic Emission Behaviour of a Low Alloy Steel		5. TYPE OF REPORT & PERIOD COVERED Technical
		6. PERFORMING ORG. REPORT NUMBER
7. AUTHOR(s) R.J. Landy		8. CONTRACT OR GRANT NUMBER(s) N00014-75-C-0419
9. PERFORMING ORGANIZATION NAME AND ADDRESS Materials Dept., 6531 Boelter Hall, University of California, Los Angeles, CA 90024		10. PROGRAM ELEMENT, PROJECT, TASK AREA & WORK UNIT NUMBERS
11. CONTROLLING OFFICE NAME AND ADDRESS Physics Program, ONR 800 N. Quincy St., Arlington, VA 22217		12. REPORT DATE May 1979 13. NUMBER OF PAGES 113
14. MONITORING AGENCY NAME & ADDRESS(if different from Controlling Office)		15. SECURITY CLASS. (of this report) 15a. DECLASSIFICATION DOWNGRADING SCHEDULE

16. DISTRIBUTION STATEMENT (of this Report)

Unlimited

DISTRIBUTION STATEMENT A
Approved for public release
Distribution Unlimited

17. DISTRIBUTION STATEMENT (of the abstract entered in Block 20, if different from Report)

18. SUPPLEMENTARY NOTES

A thesis submitted in partial satisfaction of the requirement for the M.S. degree in Engineering.

19. KEY WORDS (Continue on reverse side if necessary and identify by block number)

Acoustic Emission
A 533 B Steel
Plastic Deformation
Heat Treatment Effects
Fracture Testing

20. ABSTRACT (Continue on reverse side if necessary and identify by block number)

See pages x and xi

DD FORM 1 JAN 73 1473 EDITION OF 1 NOV 65 IS OBSOLETE
S/N 0102-LF-014-6601

SECURITY CLASSIFICATION OF THIS PAGE (When Data Entered)

TABLE OF CONTENTS

	Page
LIST OF TABLES	v
LIST OF FIGURES	vi
ACKNOWLEDGEMENTS	ix
ABSTRACT OF THESIS	x
CHAPTER 1 - INTRODUCTION	1
1.1. General	1
1.2. Basic Studies	2
1.3. Theoretical Attempts	6
1.4. Heat Treatment Effect	9
CHAPTER 2 - STATEMENT OF PURPOSE	13
CHAPTER 3 - EXPERIMENTAL PROCEDURES	15
3.1. Material	15
3.2. Test Specimens	15
3.3. Heat Treatments	16
3.4. Testing Methods	17
CHAPTER 4 - ACOUSTIC EMISSION SIGNAL CHARACTERIZATION	20
4.1. General	20
4.2. Amplitude Distribution	21
CHAPTER 5 - RESULTS AND DISCUSSION	27
5.1. Microstructures	27
5.2. Tensile Tests	30
5.3. Compact Tension Tests	45
CHAPTER 6 - CONCLUSIONS	51
REFERENCES	53

Accession For
NTIS GRA&I ✓
DDC TAB
Unannounced
Justification
By
Distribution/
Availability Codes
Dist | Avail and/or special
A

LIST OF TABLES

Table		Page
1-1	Typical cooling rates for plates of various thickness.	59
3-1	Chemical composition of A533 B Cℓ 2 steel.	60
3-2	Heat treatment schedule.	61
5-1	Mechanical and acoustic emission properties of tempered as-received steel.	62
5-2	Mechanical and acoustic emission properties of miscellaneous heat treatments.	63
5-3	Amplitude distribution exponents, m, from tensile tests of quenched and tempered steels.	64
5-4	Amplitude distribution exponents, m, from tensile tests of normalized and tempered steels.	65
5-5	Amplitude distribution exponents, m, from tensile tests of miscellaneous heat treatment.	66
5-6	Acoustic emission during necking in the tensile tests.	67
5-7	Mechanical and acoustic emission properties from the compact tension tests.	68
5-8	The characteristics of AE signals from the compact tension tests.	69
5-9	The amplitude distribution exponents, m, from the compact tension tests.	70
5-10	Fracture surface characteristics of heat treated compact tension samples.	71

LIST OF FIGURES

Figure		Page
1.1	A typical transient measured with a calibrated broad band system.	72
3.1	Dimensions of tensile specimens.	73
3.2	Orientation of tensile and compact tension specimens with respect to the supplied plate.	74
3.3	Dimensions of compact tension specimens.	75
5.1	Micrograph of the normalized condition.	76
5.2	Micrograph of the as-received condition.	76
5.3	Continuous-cooling-transformation diagram for A533B steel.	77
5.4	Tensile properties of martensitic A533B steel as a function of tempering temperature.	78
5.5	Tensile properties of bainitic A533B steel as a function of tempering temperature.	79
5.6	The reduction in area at fracture for normalized and quenched A533B steel as a function of tempering temperature.	80
5.7	AE RMS voltage and stress against time for normalized A533B steel.	81
5.8	AE RMS voltage and stress against time for the normalized plus 500°C temper condition of A533B steel.	82
5.9	AE RMS voltage and stress against time for the normalized plus 650°C temper condition of A533B steel.	83
5.10	AE RMS voltage and stress against time for the quenched plus 500°C temper condition of A533B steel.	84

Figure		Page
5.11	AE Event Counts for martensitic steel as a function of tempering temperature.	85
5.12	AE Event Counts for bainitic steel as a function of tempering temperature.	86
5.13	Schematic drawings of AE RMS voltage and stress against strain for different yielding conditions.	87
5.14	The maximum RMS level, V_r^P, for martensitic steel as a function of tempering temperature.	88
5.15	The maximum RMS level, V_r^P, for bainitic steel as a function of tempering temperature.	89
5.16	The integrated RMS level, $\overline{V}_r$, for martensitic steel as a function of tempering temperature.	90
5.17	The integrated RMS level, $\overline{V}_r$, for bainitic steel as a function of tempering temperature.	91
5.18	Integrated $\overline{V}_r^2$, against tempering temperature for quenched and tempered steel.	92
5.19	Integrated $\overline{V}_r^2$ against tempering temperature for normalized and tempered steel.	93
5.20	Stresses, σ_{YS}, σ_P, σ_{AE}, and σ_B against tempering temperature for martensitic steel.	94
5.21	Stresses, σ_{YS}, σ_P, σ_{AE}, and σ_B against tempering temperature for bainitic steel.	95
5.22	AE RMS voltage and stress against microstrain for normalized A533B steel.	96
5.23	AE RMS voltage and stress against microstrain for normalized plus 600°C tempered A533B steel.	97

Figure		Page
5.24	Typical amplitude distribution from yielding during a tensile test.	98
5.25	Typical amplitude distribution from initial work hardening region of a tensile test.	98
5.26	AE RMS voltage and load against time for the normalized compact tension sample.	99
5.27	AE RMS voltage and load against time for the quenched plus 400°C tempered compact tension sample.	100
5.28	Fractograph showing cleavage in the full annealed condition tested at 25°C.	101
5.29	Fractograph showing dimple formation in the quenched plus 700°C tempered condition tested at 25°C.	101
5.30	Fractograph showing the stretch zone formation in the as-received condition tested at 25°C.	102
5.31	Fractograph showing the stretch zone formation in the normalized plus 400°C tempered condition.	102
5.32	Typical amplitude distribution for loads up to P_Q.	103
5.33	Typical amplitude distribution for loads above P_Q.	103

ACKNOWLEDGEMENTS

I wish to thank all those whose help assisted me in attaining this goal. I would like to especially thank:

Professor Kanji Ono, my committee chairman, for his uncompromising and constructive criticism.

Professors R. Stern and A.H. Shabaik for serving on my committee and for their helpful suggestions.

Lucie Rodriguez for her patience and excellent typing.

I am also indebted to my colleagues Dr. Mamoru Shibata, Russell A. Lund, Shuh-Yueh Simon Hsu and Mitsumasa Yamamoto for their aid and advice.

Finally, I would like to express my thanks to the Office of Naval Research, Physics Program, for financial support under contract N0014-75-C-0419 and to Nippon Steel Corporation, in particular, Messers. Y. Wakamatsu and T. Suzuki of the Los Angeles Office, for supplying the steel.

ABSTRACT OF THE THESIS

Acoustic Emission Behaviour of
a Low Alloy Steel

by

Robert James Landy

Master of Science in Engineering
University of California, Los Angeles, 1979
Professor Kanji Ono, Chairman

Acoustic emission has become an important nondestructive evaluation technique, especially for pressure vessels. In the fabrication of heavy section pressure vessels, the materials experience various heat treatments which result in heterogeneous microstructures. Therefore, a program was undertaken to characterize the acoustic emission response to these variations in the microstructure of pressure vessel steel, namely, ASTM A533B steel. This data is intended to provide a base for evaluating field testing results and simultaneously to enhance the understanding of acoustic emission sources in martensite and bainite during deformation and fracture.

The acoustic emission from tensile tests were analysed using RMS voltage level, event counts, and on-line amplitude distribution. The tensile test data was used to characterise the acoustic emission response to plastic deformation. The acoustic emission parameters evaluated show separate trends with tempering temperatures following quenching or normalizing. It was observed that acoustic emission signal intensity is less for martensite than bainite, but tempered bainite produces weaker acoustic emission intensity than tempered martensite. A model was used to analyse the observed behaviour

and achieve some success in relating acoustic emission source characteristics to microstructural variables.

The acoustic emission from crack propagation was evaluated using event counts and amplitude distribution. It was found that heat treatment has a strong influence on fracture mode. Amplitude distribution also shows promise in revealing the stages in crack initiation and propagation. Further work is needed to elucidate some of the anomalies in the results of these tests.

1. INTRODUCTION

1.1. General

Acoustic Emissions (hereafter referred to as AE) are transient stress waves released during local instabilities in solids "undergoing some form of deformation". This definition of the AE phenomena is somewhat limited owing to the very wide application of AE testing in such diverse fields as engineering, geology, materials research, medicine and veterinary science, but it is sufficient for the work to be discussed here

Use of AE testing in the engineering field includes the assessment of the structural integrity of large structures, monitoring of welding, rolling and other fabrication processes, and valve leakage. In particular, AE testing accompanying the initial and in-service proof tests of large pressure vessels has become a standard method providing valuable and supplementary inspection to extensive radiographic (RT), ultrasonic (UT), and surface inspection techniques.

Included here are nuclear reactors, product storage vessels, spheres, catalytic reactors, heat exchangers and pipelines [1]. Most of the reported activity has occurred in the nuclear, chemical, petroleum, and aerospace industries although many applications in the transportation, manufacturing, and utility industries have also be reported [2]. Acoustic Emission differs for most other non-destructive testing methods in two significant respects. First, it is a passive method that depends on redistribution of internal

stresses in the object being monitored to provide the energy that is detected. Secondly, latent defects that enlarge under an applied stress are likely to be active sources of AE [2]. A limited ability to quantitatively characterize and interpret AE response data inhibits the potential for exploiting the application at the present time. The following sections are presented to give a general assessment of AE sources by reviewing basic studies, current theoretical attempts to model AE, and effect of heat treatment on AE.

1.2. Basic Studies

Generation of AE occurs during plastic deformation and must intrinsically arise from dynamic dislocation behaviour. Studies of AE sources have used both single crystals [3,4,5,6] and polycrystalline materials [4,5,6,7]. The work on single crystals is important as the effects of grain boundaries on plastic deformation are eliminated. Results of the work on single crystals of LiF, NaCℓ and Zn suggested that AE count rate is proportional to the time derivative of the mobile dislocation density [3]. Etch pit data in the near-vicinity of yield established that the computed maximum pulse rate possible from the creation of mobile dislocation line lengths by multiplication was an order of magnitude less than that observed. Therefore, dislocation breakaway from pinning points was considered to be a reasonable physical model for AE generation. Using measured dislocation densities, the length of dislocation line which was involved in the generation of an AE pulse, was estimated as a few thousand centimeters. This represents one hundredreth of 1% of the total

existing dislocation length. One AE pulse results from several simultaneous breakaway events and the propagation of these events triggers others.

This proposition provides rationale for explaining discontinuous slip, jerky dislocation motion and slip band formation. Internal friction measurements, along with AE, were used to analyze the deformation of copper single crystals [4]. Two types of AE were recorded during the compressive deformation of Cu single crystals. Burst emission was found before and after macroscopic yield while continuous emission was always initiated at the macroscopic yield point. From the frequency dependence of ultrasonic attenuation and by application of the Granato-Lucke theory of dislocation damping, parameters such as the dislocation density and segment length were calculated.

From these studies, the process of plastic deformation may be described as follows. As the external stress increased, the dislocations tend to be freed from foreign atoms and the segment length of mobile dislocation begins to increase to a critical value. As this critical value is reached, multiplication of mobile dislocations takes place suddenly and crystal yields macroscopically. After yielding, the segment length remains almost constant at small plastic strains. During unloading the AE signal intensity decreases, while measurements show the dislocation density remaining constant while segment length decreases. Hence, AE generation is dependent on segment length for constant dislocation density.

The AE pulses are generated when the multiplication of mobile dislocations takes place and a possible source may be the dynamical activation of Frank-Read sources [4]. The existence of discrete AE pulses strongly suggests that yield and plastic flow occur discontinuously. It was also shown that the strength of pinning points determines at what stress AE appears. The effects of solute concentration and orientation dependence on AE have been studied using single crystals of Aℓ and Aℓ-Mg solid solution [5].

In Aℓ single crystals, the AE behaviour was maximized at a plastic strain of 0.5-0.7%, not at yielding, and decreased gradually with further increases of plastic strain. In Aℓ-Mg solid solution, AE develops the sharp peak at the yield point, partly due to the unlocking of dislocations from solute atmospheres. The mean value of AE was approximately proportional to the inverse of the square root of the fractional concentration of Mg. This suggests mean AE was dependent on mean dislocation velocity.

In both Aℓ and Aℓ-3 at.% Mg single crystals, AE was found to be inversely proportional to the Schmid factor for a constant strain rate. Here it is thought, that the effect of the secondary slip systems of fcc materials is clouding AE behaviour associated with the shear strain rate of the primary slip system. For it was shown in hcp Zn and Cd single crystals where the active slip system very strongly predominates, the mean value of AE is directly related to the shear strain rate of the primary slip system evaluated from the inverse of the Schmid factor [5].

This dependence of AE on strain rate as well as shear strain rate was exhibited in Kieswetter's work on pure Aℓ single crystals [6]. The mean RMS* voltage level of AE was established as being linearly dependent on the square root of the strain rate. This AE strain rate dependence has been found in Aℓ polycrystals, Cu single and polycrystals. Continuous AE was also found to be a decreasing function of flow stress. For the parabolic range of the stress-strain curve the continuous emission of an annealed and an 'as-machined' specimens was found to be about the same. This coincidence of the two curves shows that the dislocation defect structure is the main parameter for the acoustic emission. Kiesewetter [6] suggested a linear relationship between the square of the RMS level and the mobile dislocation length.

Using concurrent internal friction measurements, Higgins [7] has shown for pure polycrystalline iron, that the source of acoustic emission at yield is most probably dislocation breakaway. AE in the elastic region has been shown to be consistent with magnetomechanical effect, most probably irreversible domain wall movements.

The Bauschinger effect has been studied using AE and as yet there is no agreement on the detail of dislocation related AE sources during the unloading [8,9]. The effect on AE of the grain size of polycrystalline materials (e.g. aluminum) has been explained generally in terms of internal source lengths and influence of grain boundary sources [10]. These studies have yielded the general dislocation

* RMS = Root mean square

behaviour which generates AE although the specific details are still elusive.

1.3. Theoretical Attempts

Stress waves that are emitted for sudden crack growth have been studied on the basis of elastodynamic ray theory [11], 'self-similar' solution [12], elastic field analysis [13], Green's function [14] and finite difference simulation [15]. The results of the elasto-dynamic ray theory [11], have shown mathematically, that the curved crack front causes the focussing of the radiated energy. For a crack edge of radius ρ, the surface of the focussed energy is a normal axis through the centre of the crack surface.

More surprising were the results of first-signal arrivals from crack propagation events resulting from either brittle fracture or plastic yielding at the crack. The ratio of radial displacements caused by brittle fracture (U_{BR}) and plastic yielding (U_{DR}) was found to be:

$$\frac{U_{BR}}{U_{DR}} = \frac{4c_L}{3} \quad \frac{1}{tc_L - r} \qquad (1\text{-}1)$$

where t is elapsed time, r is the distance from source to detection point and c_L is the velocity of longitudinal waves.

Experience has shown that the amplitudes of brittle fracture events are usually considerably larger than that of ductile fracture. Assuming that the amplitude is roughly proportional to the detected displacement, the suggestion arises that this only occurs for

$r/c_L + 1 > t > r/c_L$, so the displacement relationship is affected by detection position. Of course, the effects upon arrival of the head and shear components have been ignored.

Burridge [12] examined the case of an elliptical crack expanding under shear and the radiation patterns are those produced by a 'double-couple' source modified by a factor which depends on the geometry and speed of the crack. Freund [13] has shown that the associated discontinuity in mean normal stress $[\sigma]$ is:

$$[\sigma] = K_0(\pi/2r)^{\frac{1}{2}} F(x-vra^*, z, ra^*) \qquad (1\text{-}2)$$

where $[\sigma]$ is the discontinuity in mean normal stress, i.e., $\sigma_{ii}/3$ which arrives at a typical point, x, a at time $t = a^*r$, where z^* is the dilatational wave slowness and $r = (x^2 + z^2)^{\frac{1}{2}}$. K_0 is the static stress-intensity and F is an angular distribution function, where the source function is assumed to be a velocity step function of magnitude v. Pardee's solution [14] for Green's function for a plate expressed in terms of stress is important for any analytical basis for the numerical calculations of spectrally analyzed acoustic emission signals. This work has at the time of writing not been published with a comparison of actual experimental results. Tensor and spatial distribution of sources can be explored with these techniques and this holds great promise for further theoretical investigation of source functions. The finite difference simulation [15] started with a source function for the vertical displacement at the crack tip, which is similar to a step function modified to have a finite rise-time.

The calculated acceleration at the plate edge achieved a remarkable correspondence to the measured waveform for the first signal arrivals. The material under investigation was Araldite. This does not in any way reduce the significance of the assumed source function and the success of the calculations. A similar success has been achieved in tempered low alloy steel using a unique specimen geometry, the Yobell [16]. This geometry was developed to reduce interference from internal reflections of the ultrasonic pulse. Using a displacement sensitive broad-band capacitance transducer, the measured surface displacements were analysed assuming a force-step-function source and using a relation developed by Pekeris [17] and Pekeris and Lifson [18]. A typical acoustic emission transient is shown in Figure 1.1.

Firstly, the rise time of the leading edge of an AE is related to the lifetime of the source event. Secondly, the amplitude of the leading edge can be related, as a first approximation, to the magnitude F of a force-step-function source using:

$$d = 4.7 \times 10^{-2} \frac{F}{\mu h} \qquad (1\text{-}3)$$

where d is the amplitude of the lead edge vertical displacement, h is the depth of the source, μ is the shear modulus and F is the magnitude of the force step [16-18]. Thirdly, the delay of the shear wave arrival at the surface provides a method for determining the source depth. Thus the source event can be analysed with some success from the evaluation of first signal arrivals. For usual geometries of the standard tensile specimen, signal resolution is inhibited by

reflections and resonances which are caused by gauge length dimensions, curved shoulders and screw threads. Therefore, the measured intensity is not directly linked to source strength.

To facilitate identification of AE sources from signals of a piezoelectric transducer which is attached to a tensile specimen, other data analysis techniques (for example, amplitude distribution, frequency spectral analysis, event count, AE counts, RMS voltage level and energy distribution) are required. Some success for AE source identification using frequency spectral analysis has been claimed during the deformation of zirconium [19] and a low alloy steel [20]. The above mentioned parameters will continue to be used as the test specimens used also provide important engineering data, i.e., yield and ultimate tensile strengths, reduction in area, etc.

1.4. Heat Treatment Effect

Before AE application to NDE can be fully exploited, a systematic evaluation of the AE response to the heat treatment of the steels used in construction of say, pressure vessels, needs to be completed. General characteristics of these pressure vessels included the selection of thick sections and high strength alloys to be used in the construction. This latter characteristic necessitated that the rolled plate receive a quench and temper or normalized and temper heat treatment. The thickness of the plate assures a lack of homogeneity in the heat treatment. The midsection of a plate receiving a 'dip quench' experiences a significantly reduced cooling rate. Some typical values for various thickness of a 2.25%Cr-1%Mo steel are

shown in Table 1-1. [21]. The resultant microstructure is determined by the cooling rate from an austenizing temperature, and the microstructure varies with depth in the plate. The fabrication of the structure with preheating, welding and postheating heat inputs further destroys the degree of homogenization in the microstructure. In-field heat treatment of the finished pressure vessel is common commercial practice to reduce the distortion and effects of fabrication.

The material to be used in this study is a high strength low alloy steel of the ASTM A533B specification. This is an Aℓ-killed steel, which to satisfy the strength requirements, receives a quench and temper heat treatment. When quenched in thick sections, the surface microstructure consists of a tempered martensite and at mid-thickness a tempered bainite microstructure results [21,22]. Therefore, the main investigation will centre on the AE behaviour of tempered bainite and tempered martensite specimens of A533B steel.

Previous AE works have evaluated the effect of heat treatment on AE response of aluminum [8,10,23] and copper alloys [24] and steels [16,24,26]. The aluminum alloy selected for study was an AℓCuMg 2 alloy. The specimens received a solution heat treatment (495°C, 2 hours, quenched in ice water) and a subsequent ageing at 180°C for times up to 14 days. During tensile testing, two maximums were observed in the AE RMS voltage recording. The first maximum occurred at yield and the second maximum appeared during the initial work hardening stage. The signal intensity of maximum I was determined by the median free distance (i.e., average distance between particles), covered by the slip dislocations. The second

maximum was influenced by the formation of microcracks in connection with the intermetallic phases and not by the coherent or partially coherent precipitation phases formed during the artificial ageing [23]. The Cu-Ni-Si alloy upon heat treatment, precipitates a solid solution of Ni_5Si_2 intermetallic compound and copper without G.P. zones forming. The specimens received a solid solution treatment (850°C, 1 hour, water quench) then an ageing treatment at 350°C for times up to 100 hours. These treatments produced large variations in the average number of precipitated particles per unit volume, average radius of the particles, and average distance between edges of two neighbouring particles. The maximum value of the continuous AE signal was found to increase then decrease with ageing time. Acoustic energy per unit particle increased as the square of the distance between the centres of two neighbouring particles increased [24].

The AE behaviour of quenched and tempered steels was found to be complicated by the various processes that occur during the tempering of martensite. These processes included internal stress relief, formation of Cottrell atmospheres around dislocations, precipitation of epsilon and rod-shaped carbides, formation of cementite and alloy carbides, spheroidization of carbides present, recovery, and recrystallization. The maximum AE signal intensity was found to increase, decrease, then increase for increasing tempering temperatures [25]. In short, AE were found to be very sensitive to the microstructure formed by heat treatment [25,26].

As mentioned previously, the microstructures to be investigated in this study include tempered martensite so a complete description of the causes of AE will not be attempted here but left over to be discussed with the experimental work in Chapter 5.

2. STATEMENT OF PURPOSE

The goal of this study is to correlate Acoustic Emission Behaviour with the variation in steel microstructure. In addition to the usual AE parameters, on-line amplitude distribution will be used to characterize AE signals from tests using tensile and compact tension specimens. The former specimen type was selected to facilitate the study of the macroscopically elastic, yield,and initial work hardening regions associated with a simple tension test. The latter was selected to investigate initiation and the progression of such fracture mechanisms as ductile tearing, rupture and brittle crack propagation.

A review of recent mathematical models and their prediction of amplitude distribution of continuous and burst type emissions is presented to provide a background from which to analyze the results recorded experimentally.

Implicitly, this study will pursue a metallurgical evaluation of Acoustic Emission and source mechanism. Explicitly, the variation of Acoustic Emissions with microstructure of a high strength low alloy steel, i.e., A533B, is investigated. Intuitively, the examination will include such aspects as phases, types of second phase particles and the heat treatment effect. The last aspect is of considerable interest in relation to weldments and their varying microstructures.

Microstructure studies of these samples will be performed using optical and scanning electron microscopy. In concert with the tensile samples, compact tension fracture toughness samples are to be prepared with identical heat treatments. Subsequent fractographic examinations will be performed using scanning electron microscopy and possible correlations with emission results made.

3. EXPERIMENTAL PROCEDURES

3.1. Materials

The materials used in this study were sectioned from a 163 mm (6") thick plate* which meets ASTM specifications as A533B Class 2 steel. The ladle analysis of the material is given in Table 3-1.

A brief summary of the processing of the as-supplied plate includes a 90 ton pour from a 100 ton LD Converter. The slab ingot was forged in an 8,000 ton press from a 1050 x 3000 x 4170 slab into a 539 x 4100 x 2940 mm plate. The cross rolling in a 4 high reversing plate mill resulted into a 2940 mm plate after the first step and then cut in half and rolled into a 163 x 2860 x L mm plate. The mill heat treatment included a quench after 6½ hours at 915°C and followed by a stress-relief temper at 650°C for 86 hours.

3.2. Test Specimens

Tensile Specimens

Half size (0.25" diameter), cylindrical test specimens per ASTM standard E8-69 were used to study the effect produced by various heat treatments, on the tensile and acoustic emission properties of this base material.

The geometry of the specimens is shown in Figure 3.1. Most specimens were machined with the axial direction parallel to the transverse direction of the supplied steel plate (see Figure 3.2.).

---

* Supplied by Nippon Steel Corporation

Compact Tension Specimens

Compact tension specimens of the ASTM Standard E 399-74 proportions, in Figure 3.3. were used. The crack propagation and crack plane directions were the transverse and thickness directions of the rolled plate, respectively. This is shown in Figure 3.2.

3.3. Heat Treatments

The tensile specimens were austenitized at 930°C (1706°F) for 1 hour in a vertical three-zone controlled resistance wound furnace with a vacuum of less than 1×10^{-4} torr. The vacuum was necessary to reduce the degree of surface oxidation.

After a one hour austenitization at 930°C, the specimens were water quenched (WQ) or control-cooled to room temperature (i.e., normalized, N). The period during which the control-cool was executed lasted 60 minutes resulting in a nominal cooling rate of 15°C/min. Over the temperature range 850°C to 200°C, the cooling rate did not significantly vary from 15°C/min.

The specimens were then tempered in the same furnace at temperatures in the range 300°C to 750°C for a period of 24 hours, then furnace cooled. For tempering conditions at 100°C and 200°C, an oil bath and a salt bath were used respectively. The specimens were air-cooled after these treatments.

Temperatures in the austenitizing and tempering heat treatments were kept to within ± 5°C. The length of time under tempering was kept to within ± 2 hours.

A detailed tempering schedule is tabulated in Table 3-2. Some isothermal tempering treatments were also included for comparison purposes. For the same reason, some tempering times approached 50 hours.

The compact tension specimens received a similar heat treatment procedure but not all conditions were duplicated. Those that were used are marked by CT in Table 3-2.

3.4. Testing Methods

All tensile tests were conducted on a floor mounted Instron Universal testing machine. Results were recorded as load vs. time curves (which, through cross-head speed and chart speed is equivalent to a load deflection curve). Tests were conducted at room temperature and cross-head speed of 0.021 mm/sec, (0.05 in/min), or a nominal strain rate of 6.7×10^{-4} sec^{-1}. The initial and final diameters of the tensile specimens were measured with a Vernier caliper.

Acoustic Emission tests were performed using a combination of AE transducers. In the initial tests, two transducers, one resonant type and the other a broad band type, were attached to a specimen. The former is a narrow band resonant type transducer AC 175L (175 kHz fundamental frequency manufactured by Acoustic Emission Technology Corporation (AET), Sacramento, California). The latter was based on a UCLA design using a 3 MHz compressional mode PZT-5 element (6.3 mm diameter). Both were mounted on each end of the round tensile specimen with a viscous resin. Preamplifiers

(Model 160, AET Corporation) with 125-250 kHz and 30-2000 kHz filter plug-ins were used for the narrow band and broad band transducer, respectively. The input noise levels were 1.2 μV and 3.2 μV, respectively. Preamplifier was powered by a UCLA designed power supply. Other signal processing units included a HP* 3400A RMS volt meter monitoring the preamplifier output and a video tape recorder (Sony AV-3650, modified by AET for AE signal recording), for signal storage and play-back. On-line amplitude distribution analysis of AE signal was performed using an analyser (Model 203, AET) from which the outputs for the event counts summation and amplitude distribution were taken for display on an HP 2FA two pen recorder and HP 175A cathode ray oscilloscope, respectively. The amplitude distribution was permanently recorded by an oscilloscope-mounted camera. Some tests were also recorded on a 7-channel Bell and Howell VR-3700A instrumentation recorder (FM mode, 0-500 kHz). The RMS and load vs. time curves were displayed on a two-pen Soltec recorder. The event-counts and load vs. time were displayed on a two-pen 2FA recorder. Scale on both time axes was 0.4 mm/sec. (1 inch/min.).

For compact tension specimens, the electronic instruments did not differ from those described earlier. The signal from a clip gauge was used to drive the x-axis of the HP2FA recorder. In this case, the load and event counts vs. clip gauge displacement were plotted. The knife-edges were glued to the compact tension specimen using a commercial resin. The clip gauge response was found to be linear over the range 4.8 mm (0.19 in.) to 7.9 mm (0.31 in.) and the initial knife edge

---

* HP = Hewlett Packard

spacing was made approximately 4.8 mm (0.19 in.). The cross-head speed for the compact tension tests was 0.021 mm/sec., (0.05 in/min.).

Total amplification between transducer and inputs to amplitude distribution analyser (AET Model 203) and RMS voltmeter is 60 dB for all tests. The model 203 analyser obtained event counts instead of the more commonly used AE (or ringdown) counts. This eliminates the effect of the large count associated with the ringdown of a high amplitude event.

The maximum count rate from the analyser was experimentally determined as 2.3 kHz. Electronically, the model 203 analyser scans the incoming signal and counts the initial amplitude of an AE event and stops counting until the level of the signal reaches the detectable threshold again. This level is set at 10 mV for all tests. If the signal level does not fall to this threshold level, the 203 analyser starts counting after a preset time delay, which is estimated as approximately 0.4 milliseconds.

In an attempt to eliminate any sources of extraneous emission, such as the distortion of the threads and surface oxidation formed during heat treatment, the specimens were polished with grades 320 and 600 silicon carbide paper, and the threads cleaned by application of a 1/2 inch die. As a further precaution, the threads were wrapped with Teflon tape to reduce extraneous noise.

4. ACOUSTIC EMISSION SIGNAL CHARACTERIZATION

4.1. General

The advantages of using AE parameters such as Event Counts, RMS level (V_{rms}), corrected RMS level (V_r), and integrated V_r and V_r^2 are discussed as well as a survey of amplitude distribution.

The RMS voltage, V_{rms}, is a convenient measure of AE signal intensity. It is qualitatively comparable to a count rate measurement, but more importantly, it includes low amplitude signals below the detectable threshold of the AE counting system.

The RMS voltage, V_{rms}, is measured as a mean value over an averaging time, and as a result is relatively insensitive to a few AE events occurring over the averaging time. Burst-type AE is also described satisfactorily if its rate of occurrence is high [27].

When the signal intensity is less than twice that of the background noise which is an inherent property of the electronics used, the observed values of V_{rms} must be corrected for the presence of this noise. Since the noise and AE signals are uncorrelated, V_{rms} and V_r are related as follows,

$$V_r^2 = V_{rms}^2 - V_{Bkgd}^2 \qquad (4\text{-}1)$$

where V_r is the correct RMS level and V_{Bkgd} the noise level of the AE data collection system. This corrected signal intensity is required for accurate analysis of experiments exhibiting low amplitude emission frequently associated with plastic deformation. The square of V_r is

proportional to the power of AE signals over the bandwidth of the instrumentation system, necessarily modified by the resonance characteristics of the transducer used and specimens, under test. The integration V_r^2 can provide information on the total power of AE events.

Integration of V_r is conveniently determined from experimental recordings of the DC voltage output from an RMS voltmeter. The integration of V_r compares qualitatively to the total count measurement. This is especially advantageous when the rate of AE events is very high or when high and low amplitude AE signals are present during the course of measurement [27]. In either case, some information is lost by using only counting techniques whether through count saturation or too large a threshold setting.

4.2. Amplitude Distribution

The approach in the past has relied very heavily on empirical laws as the accurate modeling of the AE signal has met with very limited success. The signal variation caused by the transducer response being the major inhibiting factor. Recently, this transducer response, R_{max}, was related to the mechanical stimulus by parameters such as pulse magnitude S and duration T. Here, the two governing assumptions included that the electrical signal generated by the transducer be approximated by a damped sinusoid and the mechanical stimulus is represented as a rectangular pulse. For a small T, the magnitude of R_{max} is given as [28],

$$R_{max} = \frac{S(1 - e^{-\beta T + i\omega_o T})}{\beta - i\omega_o} \simeq S.T \qquad (4\text{-}2)$$

where ω_o is the transducer resonant frequency, β is a decay constant and i^2 equals -1. This value R_{max} corresponds to the peak amplitude of a burst emission signal, V_p. Results have shown that the peak voltage, V_p, increases linearly with the pulse duration T in accord with Eq. (4-2) [28]. The energy of the mechanical stimulus is given by,

$$E_s = \int_{-\infty}^{\infty} s^2(t)dt = S^2T \qquad (4\text{-}3)$$

where s(t) is assumed to represent the surface displacement or velocity. For constant pulse duration and varied pulse height, Eq. (4-3) yielded

$$E_s \propto S^2 \propto (R_{max})^2 = V_p^2 \quad . \qquad (4\text{-}4)$$

For constant pulse height and varying pulse duration, the following result is obtained,

$$E_s \propto T \propto R_{max} = V_p \quad . \qquad (4\text{-}5)$$

The above analysis showed that the proportionality between E_s and V_p^2 holds only when all the events have an identical pulse duration. Unless this condition is met the oft-quoted relation of Eq. (4-4) cannot be justified. The second case applied for small values of T but the conditions are physically realizable [28]. This may indeed represent an approximation to continuous AE signals.

Burst emission signals cannot be represented so easily and an analysis must include the nature of the counting techniques. With the transducer electrical signal modeled as before, the number of AE counts per event, n_e is given by,

$$n_e = \left(\frac{f_o}{\beta}\right) \ell n \left(\frac{V_p}{V_t}\right) \qquad (4\text{-}6)$$

where f_o ($= \omega_o/2\pi$) is the resonant frequency and V_t is the threshold voltage. The cumulative amplitude distribution of AE counts per unit time (or AE count rate) $\dot{N}$ is then given as an integral [29],

$$\dot{N} = \int_{V_t}^{\infty} N_p(V_p) \cdot n_e(V_p, V_t) dV_p \qquad (4\text{-}7)$$

where N_p is the distribution of peak amplitudes, V_p. Calculation of N_p from $\dot{N}$ is very difficult when using the AE counting technique, as a result of the influence of n_e. Assuming that the burst emission peak distribution N_p is of the Rayleigh type, the AE count distribution is semi-logarithmic in form, i.e.,

$$\dot{N} = c_1 \exp(-\alpha V_t) \qquad (4\text{-}8)$$

where c_1 and α are constants. Similar results were achieved by either a Gaussian distribution with zero shift or the Poisson distribution being substituted in N_p. It appears likely that the superposition of burst emissions is the origin of the observed distribution of Eq. (4-8) [30]. Another model for specifying a peak amplitude distribution assumed a power law relationship that is often used in earthquake engineering [31,32]. This model is,

$$N_p(V_p) = k V_p^{-b} \qquad (4\text{-}9)$$

where k is the total number of emissions acquired using the threshold voltage V_t and b is the exponent. The number of AE counts $N(V_t)$ is given by,

$$N(V_t) = \frac{k\, f_o\, \tau^*}{b}\, V_t^{-b} \qquad (4\text{-}10)$$

where τ^* is the time the signal rings down to the threshold voltage[31].

All the previously derived distributions involved AE counts whereas the event count distributions would have larger exponent values when using the same peak amplitude distributions. This results from the weighting in favour of the higher amplitude events that arises when AE counts are used. This weighting is absent in the event count technique. The event count method also reduced the difficulty in extracting N_p from $\dot{N}$ since n_e equals 1 in Eq. (4-7). Evans [33] using Eq. (4-9) as a starting point and applying extreme value statistics has arrived at the cumulative probability function, F(V), for burst AE given by,

$$F(V) = 1 - e^{-(V^*/V)^b} \qquad (4\text{-}11)$$

where V^* is a constant for a particular detection system. This equation reduces to the form of Eq. (4-10) at large V.

The AE produced in fracture toughness tests is often well represented by the power-law distribution of Eq. (4-10). In these tests, there are two separate distributions. At the lower amplitude region, the exponent value is close to 3 (i.e., plastic deformation) while the exponent value in the higher amplitude region is in the

range 0.3 to 1.6, (i.e., crack propagation), when using an event count analyser. This has been experimentally observed on A533B [34] and 1%Cr-Mo-V [35] steels.

The modeling of continuous emission was approached using Rice's theory of random signal analysis and the assumption that the continuous type AE signals were stationary and Gaussian [29]. This leads to the amplitude peak distribution of the form,

$$N(V_p) = A \exp(-V_p^2/2) \qquad (4\text{-}12)$$

where A is a constant. It was shown that a narrowband random signal results in the Rayleigh distribution, whereas a broadband signal gives the Gaussian distribution. Counting all peaks above a threshold value, AE count rate $\dot{N}$ can be described by [29],

$$\dot{N} = n_o \exp(-V_t^2/2V_{rms}^2) \qquad (4\text{-}13)$$

where n_o is a constant that depends on the bandwidth of the signal, V_t is the threshold voltage and V_{rms} is the RMS voltage of the signal. A similar distribution function to Eq. (4-12) was also derived by representing continuous AE signals by a special non-stationary random process, consisting of the product of a slowly varying deterministic function with a stationary Gaussian random process [36]. The Eq. (4-13) can be applied with some confidence, not only because it was derived satisfactorily but has been experimentally confirmed during plastic deformation of 2024 aluminum alloy [23], several copper alloys [37,38] and HSLA steels [28].

During tensile deformation of a C-Mn steel, it was shown that m equal to 4 in the following relationship represented plastic deformation at yield very well [28],

$$N_e = A \exp(-B V_p^m) \qquad (4\text{-}14)$$

where A and B are empirical constants and N_e are event counts. Burst emission generated by decohesion of the MnS inclusions during the latter part of tbe same tensile tests had exponent values, m, in the range 0.2 to 0.35 [28]. Generally, burst emissions produce lower valued exponents than the continuous signals generated at yield.

In conclusion, the amplitude distribution of burst emission can be expressed successfully using either power law or exponential law relationships but continuous emission has been established as following a Gaussian distribution with an exponential relationship between counts and V_p [29,31].

5. RESULTS AND DISCUSSION

5.1. Microstructures

The microstructure of the normalized condition is auto-tempered bainite. The auto-tempering occurred as the start of the bainite transformation begins well above room temperature. An optical micrograph of the normalized condition is shown in Figure 5.1. The quenched sample exhibited a lath-type auto-tempered martensite frequently found for steels with 0.20% C content. The martensite laths are grouped in larger sheaves or packets. The as-received condition is ferrite and carbide mixture. The long tempering time at 650°C causes the carbide to coarsen [39]. The position from which the specimen was cut in the original thick plate will determine whether the starting microstructure was martensite or bainite. The former is present close to the plate's surface and the latter is found at positions near to the centre of the plate. Figure 5.2 shows a typical micrograph for the as-received condition.

The isothermally transformed condition resulted in a microstructure consisting of large areas of ferrite and coarse pearlite. The full anneal treatment created a mixture of ferrite, pearlite and bainite, as is shown in Figure 5.3, the Time-Temperature-Transformation (TTT) diagram for continuously cooled specimens [22].

The processes that occur during the tempering of martensite and bainite will be reviewed with the aid of work published in the literature as optically there is little change discernible in the microstructure at low tempering temperatures.

The martensite dislocation substructure consists of cells with a density which is estimated to be approximately 10^{12} cm/cm^3 [40]. Since the martensite start temperature (M_s) is well above room temperature, there is a rearrangement of C atoms during the quench hence producing the auto-tempered nature of the quenched state. It has been estimated that for alloys with a 0.20% C content, 90% of the carbon was segregated to dislocations during quench [40,41]. The remainder contributed to the precipitation of ε-carbide ($Fe_{2.3}C$) during tempering at 100°C to 200°C, and has been confirmed for a 24-hour temper at 150°C by Speich [40,41].

Cementite forms in the tempering range 250°C to 700°C. The rod-shaped carbides appear at 300°C and spheroidize at high temperatures. The nucleation sites are frequently martensite lath boundaries at low temperatures and ferrite grain boundaries at higher temperatures [40,41].

Above 400°C, recovery and recrystallization of the dislocation substructures and the precipitation of alloy carbides (Mo_2C, etc.) occur. Recovery is important between 400°C and 600°C, where the cell boundaries and random dislocations contained between them are annihilated, and a fine-grained, acicular structure is developed. Recrystallization generally occurs above 600°C. It has been shown for a steel of similar composition, the Fe_3C particles coarsen but the softening is retarded by the formation and fine dispersion of needle-like Mo_2C precipitates at 500°C [42,43]. The fine size and dispersion of Mo_2C and $M_{23}C_6$ particles are direct results of the lower diffusivity of substitutional alloying elements. Also, these form initially as

coherent precipitates primarily, on dislocations inherited from the as-quenched martensite [43]. After the recrystallization is completed, the growth of Fe_3C spheroids and "defect-free" ferrite grains continued along with the sub-grains, and followed a $(time)^{1/3}$ relationship[43,44].

The normalized bainite is a mixture of an acicular bainitic ferrite and carbide. The density of dislocations was shown to be very high in the bainitic ferrite [45] and is estimated to be in the range of 10^{10} lines/cm^2 [46]. Electron microscopy study of A533B steel cooled at 10°C/min., (slightly less than the rate used in this study) showed an acicular structure with carbides. Köster peaks of internal friction measurements of bainitic structures have shown that considerable interstitially dissolved C-dislocation interactions take place but were found to be less than similar interactions in martensite structures [47]. The mechanical properties and tempering characteristics of a 0.15%C-1-1/2%Mn-1/2%Mo steel have been studied extensively [43,48-51]. The hardness remains at the as-normalized value until the Holloman Tempering parameter (T_T(°K)(20+log t (hrs))) reached 18,000 which corresponds roughly to 24 hours at 600°C. Tempering temperature, T_T and time must be expressed in °K and hours, respectively. No significant decrease in yield stress is observed until 550°C due to the persistence of the acicular bainitic ferrite grains and the formation of Mo_2C precipitates in these grains. Usually, the carbides are coarser in bainite than in martensite but a finer bainitic grain size is observed for tempered steels [43,52]. Above 650°C, the carbides formed at both prior austenite and ferrite grain boundaries. At 700°C, the same processes apply as discussed previously for martensite.

It has been observed that the tempering of normalized and quenched samples at 650°C and 700°C produced finer grain sizes and carbides in the quenched samples [39]. This influences the as-received microstructure and is expected to affect the acoustic emission behaviour.

5.2. Tensile Tests

Common engineering parameters such as yield (σ_{YS}) and tensile strengths (σ_{UTS}), and reduction in area (RA) for various tempered specimens are shown in Figures 5.4, 5.5 and 5.6. The observed values of yield strength, tensile strength, and reduction in area agree very well with those published previously in the literature [22,39]. The softening in the tempered martensite is caused by the loss of solid solution of the carbon. The ε carbide precipitation at 100°C has more than balanced this loss as the yield stress increases. At higher tempering temperatures, the recovery of dislocations and recrystallization cause the yield strength to decrease rapidly. This softening is retarded somewhat in the range 500°C to 600°C where the fine dispersion of alloy carbides is evident. The increase in the tensile strength at 700°C is not observed in the literature. The microstructure is a two phase mixture of ferrite and coarse carbide particles. This suggests that the Orowan loop mechanism is occurring during deformation and the resultant high work-hardening rate would produce a larger ultimate tensile strength. The tempering at 750°C holds the sample in the $\alpha+\gamma$ field and upon the slow cool the γ present decomposes into moderately fine pearlite. This results in a stronger microstructure

than the spheroidized carbides and defect free ferrite that are formed during the tempers at 650°C and 700°C. Accordingly, the yield and tensile strengths should be and are higher.

The hardness of the normalized specimen was found to be 57.5 R_A which compares favourably with published values. From Figure 5.5, no significant decrease in yield strength is observed until 550°C due to the persistence of the acicular bainitic ferrite grain and the formation of Mo_2C precipitates in these grains. Since recrystallization produces similar microstructures above 600°C, the yield and tensile strength data are comparable for both tempered martensite and bainite at 600°C to 700°C. The reasons for the trends are therefore similar to those discussed previously. The results of the reduction in area follow the usual increasing trends with decreasing yield stress.

Typical experimental curves of stress and RMS voltage against time are shown for various heat treatment conditions in Figures 5.7 through 5.10. The RMS voltage curve assumes a particular appearance depending on the type of yielding that occurs. Specific examples are the continuous yielding and broad AE peak in Figure 5.7 and the yield drop and many small peaks of the AE signal in Figure 5.9. This will be discussed later after a number of useful parameters have been derived. The RMS level is referenced to preamplifier input. The AE event counts recorded during the tensile tests are presented in Figures 5.11 and 5.12 for the tempered martensite and bainite, respectively. The appellation "Yield" in these and future curves

specifies that the data is collected before the yield strength is reached, while "Total" represents the complete test.

The definitions of new parameters are made with reference to the schematic drawings shown in Figure 5.13. The maximum RMS level (V_{rms}^{max}) occurs at a stress (σ_p). The values of V_{rms}^{max} were corrected for the presence of noise via Eq. (4-1) and these corrected values, V_r^P are displayed against tempering temperature in Figures 5.14 and 5.15. Selected tests also had the V_{rms} curve corrected for noise and the integration of these curves provided a qualitative view of the total intensity of AE signals produced in each test. This parameter, $\overline{V}_r$, is shown in Figures 5.16 and 5.17. The integrated value was necessary as count rate saturation was experienced in tests with very high RMS levels. The "flattened" portion in Figure 5.11 around 200°C is indicative of this. A parameter to be used later in the discussion concerns the integration of the square of the corrected RMS or $\overline{V}_r^2$. Figures 5.18 and 5.19 display the $\overline{V}_r^2$ for tempered martensite and bainite, respectively. By virtue of the squared nature of the parameter, the plot is best suited to logarithmic presentation. The integrations of the V_r and V_r^2 curves were performed by using a planimeter and numerical integrations, respectively. The onset of detectable AE is signified by the stress level, σ_{AE}. When the corrected V_r reaches an arbitrary value which is defined here as V_{Bkgd}, the stress level is denoted as σ_B. From Eq. 4-1, the V_{rms} level for V_r to equal V_{Bkgd} is found to be $\sqrt{2}\, V_{Bkgd}$. Figures 5.20 and 5.21 show a comparison of the parameters σ_{YS}, σ_p, σ_{AE} and σ_B for the samples tested. As both continuous yielding and yield drop

phenomena were observed, Figures 5.13a and 5.13b define the above parameters for the respective case. The preceding parameters for other conditions are listed in Tables 5-1 and 5-2. For the normalized and tempered examples, a yield point and Lüders band were observed for the tempering temperatures of 600°C and 650°C. All others showed continuous yielding and higher AE levels. To investigate this, two samples were normalized and one was further tempered at 600°C for 24 hours. Here, it is known that mobile dislocation density is low before yield and the yield drop is the result of the breakaway of heavily pinned dislocations and nucleation of fresh dislocations. These two samples were instrumented with strain gauges so that the RMS voltages and stress against microstrain curves could be obtained. These curves are shown in Figures 5.22 and 5.23. The important features of Figures 5.22 and 5.23, include the coincidence of the rapid rise in AE with the first deviation from a linear stress-strain curve. Also the σ_{AE} and σ_B values are lower for the normalized or continuous yielding, the dislocations are generated by cross-slip and unpinning with grain boundary source activation probable at higher stress. The high stress levels associated with a yield drop suggest that the sources of dislocation multiplication may include grain boundaries and to a less extent unpinning. The initiation of plastic deformation is accompanied by acoustic emission. Possible sources of AE during plastic deformation include the activation of dislocation sources (e.g., grain boundaries, cross-slip,etc.) and unpinning of dislocations.

The variation of AE behaviour with tempering temperature following normalization treatment must therefore include some dependence on dislocation density and strength of pinning. The broad AE peaks found at room temperature to 200°C appear to be the results of a high density of dislocations very weakly pinned. From Figure 5.21, the σ_{AE} and σ_B are among the smallest values for this range of tempering temperatures. The AE peak increases in height and in sharpness for the temperature range 300°C to 500°C. There are continuing increases in σ_{AE} and σ_B for these temperatures. Hence the dislocations are pinned more strongly but not as heavily pinned as those of the 600°C and 650°C temper conditions. Since the dislocations cannot move until higher stresses are reached and the yield strength is roughly constant up to 500°C temper, the RMS voltage curve tends to become more and more a sharp peak as shown in Figure 5.8. In 600°C and 650°C tempering range, there is a low dislocation density and these dislocations are pinned very strongly. Since the microstructure is a ferrite-carbide mixture, and very large stresses are needed to nucleate dislocations probably from the sources at grain boundaries, the AE curve is a series of small peaks which coincide with load drops on the stress curve. The low level of AE is the result of sources being confined to a localized volume around the Lüders front, instead of the complete gauge length of the specimen as is the case with continuously yielding samples. For the 700°C temper condition, the AE is a broad peak very similar to the normalized case. The large AE levels are from the large number of mobile dislocations since the nucleation stresses are very low (see σ_{AE} and σ_B). The large scatter in the σ_{AE} results is due

in part to the fact that σ_{AE} is more open to personal interpretation than other parameters such as σ_B.

The low RMS level for as-quenched martensite is related to the very high dislocation density present and the small mean free flight distance moved by these dislocations. The effect is also found in heavily cold-worked material. Yield drops and Lüders band were observed for tempered conditions at 500°C, 600°C and 650°C. Discontinuous stress-strain behaviour was also observed for the 300°C and 400°C tempers. The absence of a yield drop in these cases arises from the low effective stiffness of the load train and testing machine. The AE characteristics are similar for all tempers from 200°C to 650°C. These included two peaks appearing close to either the conventionally defined offset yield strength or the yield drop when present. Since the dislocation density, ρ, in tempered martensite is roughly constant up to the 400°C temper [41], the variation in V_r^P must be related to the stress required to nucleate mobile dislocations whether through activation of sources or the breakaway of pinned dislocations. During the tempering range, the precipitation of the ε-carbide, rod-shaped carbide and cementite takes place [40]. The effect of these processes is seen in the trends of σ_{AE} and σ_B. The σ_{AE} increases up to 500°C while σ_B appears to be constant. For tempering conditions between 500°C and 650°C, the stresses σ_{YS}, σ_B and σ_p are all comparable. Therefore, the dislocations are very strongly pinned. The dominant mechanism to emit AE in a tempered martensitic steel has been established as the nucleation of fresh mobile dislocations by multiplication and unpinning [25]. The decreasing trend in V_r^P over

the 500°C to 650°C tempering range is related to increased pinning strength and the localized effect of the Lüders band. Both effects cause a reduction in the number of possible dislocation sources. The increase in V_r^P at 700°C is accompanied by further decreases in σ_{AE} and σ_B suggesting that this increase is the result of the dislocation generation not being restricted to a localized volume, as with Lüders band.

The continued tempering of the as-received samples without an intermediate austenitizing treatment has a deleterious effect on all mechanical properties (see Tables 5-1 and 5-2). The values of V_r^P for these samples are smaller for the tempered conditions. The coarsening of the carbides is known to take place at these temperatures accompanied by growth of sub-grains. This is manifested in the decreasing values of stresses σ_{YS}, σ_P, σ_{AE} and σ_B. So for longer tempering times and higher tempering temperatures (below 700°C), the values of the AE parameters decrease. This trend was also observed in a sample tempered for 50 hours at 600°C after normalizing. Of the six tempering conditions listed in Tables 5-2 and 5-2, the phenomenon of continuous yielding was found in the full anneal and as-received plus 700°C temper conditions, while a yield point and Lüders band were observed in the others. Generally, the continuously yielding sample produced the smallest peak values of RMS voltage. This suggests that the density of mobile dislocations ρ_m is important to the RMS voltage level, as the ρ_m is known to increase very rapidly during the yield drop while ρ_m is linear with strain for small strains during continuous yielding.

The degradation of the mechanical properties of the as-received (thickness) specimen is the result of the varying microstructure and the MnS inclusions. The microstructure of a quench and tempered sample as mentioned before is a function of the distance from the plate's surface. In tests using specimens that are cut parallel to the Transverse direction of the rolled plate, the microstructure is generally the same as the whole specimen is located at the same depth from the surface. For thickness direction samples, this is not the case as the specimen's length covers half of the plate's depth. The reduction in area is affected by MnS inclusions whose broad face and longest axis are now perpendicular to the tensile axis. The inclusions initiate voids at lower stresses (strains) due to their larger stress concentration factor which is the result of the longest axis being perpendicular to the tensile axis.

In all heat-treated conditions, the dominant AE signals were of a continuous nature. Therefore, these results will be examined using a recent model [53] which was developed from the Malén and Bolin model [54]. The new model uses an approximation to the source step function by use of the Gauss error function with a rise time of 4τ. This function is given as

$$u(t) = \frac{1}{2}[\mathrm{erf}(t/2\tau) + 1] \qquad (5\text{-}1)$$

where t is time. The stress pulse at a distance r is given as

$$\sigma(r,t) = -\frac{S_m}{8\pi^{3/2} r c^2 \tau^2}\left[\frac{(r/c-t)}{2\tau} e^{-(r/c-t)^2/4\tau^2}\right] \qquad (5\text{-}2)$$

where S_m is the source strength function, i.e.,

$$S_m = 2\mu\, \Delta\varepsilon_{k\ell}\, V^* + \lambda\delta_{kk}\, \Delta\varepsilon_{mm}\, V^* \quad . \tag{5-3}$$

Here, μ is the shear modulus and λ is the Lamé constant, while $\Delta\varepsilon$ and V^* are plastic strain increment and volume, respectively. The minimum and maximum of Eq. (5-2) occur at $t = (r/c) \pm \sqrt{2}\,\tau$. The complete source function $S_{k\ell}$ is given by,

$$S_{k\ell} = S_m \cdot u(t) \quad . \tag{5-4}$$

The stress pulse is bipolar, and for the results described here the peak stress σ_{max} is given as,

$$\sigma_{max} \simeq \frac{S_m}{r\,\tau^2} \quad . \tag{5-5}$$

A narrow band transducer's electrical response to a mechanical stimulus, such as Eq. (5-2), is given by,

$$R(t) = \int_{-\infty}^{\infty} \sigma(\lambda)\, r(t-\lambda)\, d\lambda \quad . \tag{5-6}$$

Here R_{max} or peak output voltage of the transducer, V_p, may be approximated by

$$R_{max} \simeq \sigma_{max} \cdot \tau \propto \frac{S_m}{rt} \tag{5-7}$$

when τ is less than $1/f_o$. To assess the random summation of numerous AE events, N_R events are considered to occur over the

averaging time, Δt of the RMS voltmeter. Therefore, the event rate equls $\dot{N}_R$. Assuming each event produces a plastic strain increment, $\Delta\varepsilon$, the strain rate $\dot{\varepsilon}$ of the test, is given by,

$$\dot{\varepsilon} = \dot{N}_R \cdot \Delta\varepsilon \quad . \tag{5-8}$$

From Eq. (5-7), the sensor output, V_p can be given by,

$$V_p \propto \frac{\Delta\varepsilon}{\tau} \quad . \tag{5-9}$$

It was shown that continuous emission is Gaussian in nature, so N_R randomly arriving signals produce a mean output, V_r, of

$$V_r \propto \sqrt{N_R} \cdot \frac{\Delta\varepsilon}{\tau} \quad . \tag{5-10}$$

These results yield the commonly observed strain rate dependence. With $\Delta\varepsilon$ and τ constant, the V_r is given as,

$$V_r \propto \sqrt{\dot{\varepsilon}} \propto \sqrt{\dot{N}_R} \quad . \tag{5-11}$$

By squaring Eq. (5-10), N_R is given by,

$$N_R \propto \frac{V_r^2 \ \tau^2}{(\Delta\varepsilon)^2} \quad . \tag{5-12}$$

Thus, N_R may be compared by knowing the rise time, τ, plastic strain increment, $\Delta\varepsilon$ amd V_r^2. For constant $\dot{\varepsilon}$ and $\Delta\varepsilon$, the influence of rise time on V_r is found to be,

$$V_r \propto \frac{1}{\tau} \quad . \tag{5-13}$$

The effect on N_R or $\Delta\varepsilon$ for constant ε and τ can be given as,

$$V_r \propto \sqrt{\Delta\varepsilon} \propto \frac{1}{\sqrt{N_R}} \quad . \tag{5-14}$$

The rise time τ is expected to be a function of the applied stress level and the type of unpinning processes that occur. The influence of the applied stress level on τ is thought to result from the greater acceleration of dislocations to higher velocities at larger unpinning stresses. For dislocation related deformation, the plastic strain increment, $\Delta\varepsilon$, is given by,

$$\Delta\varepsilon \simeq b \cdot \Delta x \cdot \rho_m \tag{5-15}$$

where b, Δx and ρ_m are the Burgers' vector, the mean distance moved, and the density of mobile dislocations, respectively [54].

This model will be used to examine AE behaviour, for selected heat treatment conditions. These conditions include quenched, normalized and quenching or normalizing plus tempering conditions at 300°C and 650°C. The discussion will also attempt to assess the effect of microstructural features on $\dot{N}_R$, $\Delta\varepsilon$ and τ.

For tempered martensite, the V_r^P increases with tempering temperature up to 300°C, then decreases as 650°C is reached. The as-quenched condition is a lath martensite with a very high dislocation density. After 24 hours at 300°C, the microstructure is a lath martensite with rod-shaped carbide precipitates [41]. Since recovery does not occur until 400°C, the density of dislocations is essentially the same. Tempering at 650°C results in equiaxed

ferrite grains with spheroidal cementite at the ferrite grain boundaries and a fine dispersion of alloy carbides in the interior [42,43]. The as-quenched martensite has a large density of dislocations. Most of these dislocations are mobile. Thus, for a given strain, the movement of mobile dislocations need not cover large distances. In terms of the above model, N_R is large and $\Delta\varepsilon$ is very small. It appears that τ is dictated by the movement of each dislocation and is not expected to be very small. Hence, V_r^P is small. For 300°C tempering condition, the values of σ_{AE} and σ_B suggest that the dislocations are pinned more effectively. Since the internal stresses are also reduced and the pinning strength is increased, the rise time may be controlled by the unpinning of a dislocation source. With increased pinning effectiveness, the initial mobile dislocation density is reduced. The progression of these dislocations may trigger an avalanche of others, which would effectively raise $\Delta\varepsilon$. This combined with a smaller τ would increase V_r^P very significantly, according to Eq. (5-10). This agrees with the observation. For 650°C temper, the dislocations are pinned very strongly as σ_{AE} (or σ_B) is found to be very close to σ_{YS}. There is only a small density of mobile dislocations, as evidenced by the appearance of a yield point. For these to achieve a very large $\Delta\varepsilon$, which is the case with a yield drop, an avalanche effect may have to occur, and a high AE output results upon yielding. However, even the peak level of the AE output is still low compared to V_r^P of the 300°C tempered sample. It appears that the effective rise time is increased, although it is not clear why this should be so. This reduces the V_r^P.

A very similar stress-strain and AE behaviour to those just described for the 650°C case has been observed for pure iron samples.

For tempered bainite, the V_r^P increased in comparison to that of the as-normalized sample upon tempering at 300°C, but decreased at 650°C. The microstructure of the normalized and the 300°C tempered conditions are mixtures of acicular bainitic ferrite and carbides. For bainite tempered at 650°C, the same processes of recrystallization apply as for the tempered martensite so the microstructures are similar between the normalized and quenched samples. The variation of V_r^P with tempering temperature in normalized samples is not of the same magnitude as tempered martensite. The V_r^P level of the as-normalized condition is comparable to a quenched sample tempered at 600°C. The broad shape of the RMS voltage curve suggests that there is less pinning. This is indeed reflected in the values of σ_{AE} and σ_B for the respective cases. For the normalized case, σ_{AE} and σ_B are 16% and 28% of the yield strength, respectively, while for the as-quenched plus 600°C temper, the figures are 79% and 91% respectively. In both the as-normalized and as-quenched plus 600°C temper, the microstructure is acicular ferrite and carbides [39,42], but the dislocation density of the former condition is expected to be greater as the latter condition is the result of recrystallization. Therefore, the initial mobile density of dislocations is thought to be larger. From this, N_R is considered to be greater thus dictating that $\Delta\varepsilon$ is much smaller for the as-normalized case than the as-quenched plus 600°C temper condition. Since the avalanche effect is not likely to occur as the initial ρ_m is larger than the as-quenched plus 600°C temper case, the

rise time, τ, for the as-normalized case is believed to be smaller. This is apparently able to produce comparable V_r^P levels for both cases. For the normalized plus 300°C temper condition, both σ_{AE} and σ_B are 67% of the yield strength indicating the dislocations are pinned more effectively than the as-normalized case. Therefore, $\Delta\varepsilon$ is increased as the initial ρ_m and thus the N_R decrease because of this pinning. A larger $\Delta\varepsilon$ should yield an increased V_r^P level as is observed in Figure 5.15. The same arguments for the as-normalized plus 650°C temper apply as previously discussed for the same tempering condition on martensite. It is important to note that the lower values of V_r^P at the 200°C tempering condition (c.f., Figure 5.15) has eluded explanation as optically there are no discernible differences in the microstructures up to 600°C. Transformation kinetics also predict limited changes in the microstructure for this tempering range.

In summary, the trends of $\dot{N}_R$, $\Delta\varepsilon$ and τ with tempering were used following Eq. (5-10) to predict the observed variations in V_r^P. It was suggested that $\dot{N}_R$ and $\Delta\varepsilon$ are related to the microstructural features found, and τ is closely coupled to the strength of dislocation pinning.

The experimentally derived amplitude distributions were fitted with curves of the form of Eq. (4-14) and the exponents, m, evaluated. The values of m from these tests are listed in Tables 5-3 and 5-4. At yielding, the exponents' values vary from 2 to 4. The former describes the Gaussian nature of continuous emission. The latter arises from the truncation that occurs at high RMS levels in the event count analyser. The yielding in both tempered martensite and

bainite produced similarly valued exponents. The conditions which are marked with an asterisk, are the results which were taken with a broadband transducer not the resonant transducer. This appears to result in the lower value of the exponents. In the initial work-hardening regions, the amplitude distribution is made up of two distinguishable parts. Figures 5.24 and 5.25 show typical amplitude distributions from yielding and the work-hardening regions of a tensile test. The value of the lower amplitude region indicates that its origins lie in the same processes as yielding. The higher amplitude region has exponents of the range 0.5 to 4. These are lower than those due to yielding but are larger in exponent value than those distributions that are known to originate from inclusion decohesion[28]. A possible source for the second distribution with m in the range 0.5 to 1 is the cooperative movement of dislocations in cell walls [55]. Table 5-5 lists the exponents from tests on the tempered as-received samples and others. The exponent values from samples with a broadband transducer (i.e., marked with *) are smaller as before. The RMS voltage signal from the as-received (thickness) sample contained many burst emissions. The amplitude distribution exponents are similar to distribution arising from inclusion decohesion. This has been observed in thickness direction samples of other low alloy steels [28].

Some emissions were collected during the necking of the tensile specimens. Table 5-6 shows the results of the tests from the same heat treatment. In tests on the same microstructure, the emissions were found in one test, but not the others, and this occurs frequently. Burst emissions have been observed during the necking of tempered low

alloy steel specimens and have been thought to arise from fast shear linage of interinclusion voids [16]. The latter required a low work hardening capacity. The yield to tensile strength ratio, n_y, which is used to estimate work hardening capacity, is listed in Table 5-6 also. There appears no correlation between n_y and AE behaviour during necking. This combined with the inconsistency of results on the same microstructure suggests that much of the emissions may be spurious in nature.

5.3. Compact Tension Tests

The acoustic emission from the initiation and propagation of cracks was studied using compact tension specimens of differing heat treatments. These heat treatments are listed in Table 3-2. Test parameters included event counts, RMS voltage levels and load against time curves. Typical test records of RMS voltage level and load against time are shown in Figures 5.26 and 5.27. Load against clip gauge displacement (CGD) curves were also recorded enabling the evaluation of fracture toughness. The load, P_Q, corresponding to 2% increment of crack extension is normally established by 5% deviation from the linear portion of the load vs. CGD curves. This load is used to calculate the fracture toughness. Aside from one as-received specimen with a 127 μm (0.005 in) notch radius, the samples were precracked prior to testing. The maximum precrack and test loads are defined as P_{fmax} and P_{max}, respectively. All the fracture toughness tests were found to be invalid according to the ASTM specification E399-74. Therefore, the fracture toughness value that is obtained

from P_Q is not plane strain fracture toughness, K_{Ic}, but the apparent fracture toughness, K_Q. To satisfy plane strain fracture conditions, the specimen thickness was found to be 80 mm (3.2 inch) or greater which exceeds the 19 mm (0.75 inch) specimens that are used here. The event counts that are acquired up to loads P_Q and P_{max} are defined as $N_e(P_Q)$ and $N_e(P_{max})$, respectively. Since the predominant AE signal was observed to be of the burst type, the event count represents a more effective comparative parameter than the maximum RMS voltage level. These parameters P_Q, P_{max}, P_{fmax}, K_Q, $N_e(P_{max})$ are listed in Table 5-7. The yield strength, σ_{YS}, found from the tensile tests is listed together with the respective heat treatment. The type of AE observed with the RMS voltage curves is listed against the load ranges of the test in Table 5-8. The first column is the emission type observed during the loading from zero to the maximum precrack load, P_{fmax}. The second, third and fourth columns are the load ranges from P_{max} to P_Q, P_Q to P_{max} and P_{max} to end of test, respectively. Usually, when P_Q and P_{max} are reached, the observed AE is characterized by numerous signals having large to very large amplitude. The amplitude exponents, m, are also listed against the loading range, in which the distributions were acquired during the test (see Table 5-9).

The fracture surfaces were cut from the compact tension specimens and cleaned ultrasonically in an acetone bath. These surfaces were observed using a scanning electron microscope and the features seen are listed in Table 5-10 along with remarks from visual observations of the specimens. Some of these scanning electron microfractographs are shown in Figures 5.28 through 5.31.

Since the heat treatments of the compact tension samples are very similar to the tensile test specimens, the microstructures are considered the same. It is appropriate to re-examine these microstructures. The full anneal heat treatment produces a mixture of ferrite, coarse pearlite and tempered bainite due to the low cooling rate. The as-received condition is a combination of large areas of ferrite and tempered bainite. The normalized specimen contained tempered bainite. The normalized plus 400°C tempered condition has no discernible differences from the normalized condition, optically. It is thought, however, there may be some recovery of the dislocation substructure as a result of the long tempering time. After tempering at 700°C for 24 hours, the microstructure of the initially normalized sample is a mixture of ferrite and coarse carbides. The as-quenched condition was an auto-tempered lath martensite. The as-quenched plus 400°C temper condition is a lath martensite with spheroidized carbides. The dislocation substructure has been eliminated by the recovery processes that have been observed at this tempering temperature [41]. The as-quenched sample tempered at 700°C has a similar microstructure to that discussed previously for the normalized plus 700°C tempered condition.

From Tables 5-7 to 5-8, the conditions which exhibit continuous AE signals also have very large values of event counts $Ne(P_{max})$. These conditions include, in descending order, as-received with the blunt notch, the full anneal, quenched and normalized plus 400°C tempers. For the as-received condition with the blunt notch, the continuous signals probably arise from the expansion of the plastic

zone and the fibrous crack growth as evidenced by the thumbnail shaped area of dimple formations (see Table 5-10). It was observed in the tensile tests that conditions which exhibited large RMS voltage levels also give rise to a large number of event counts. In the previously mentioned conditions, both continuous signals and dimple formation in the stretch zone were observed (see Tables 5-8 and 5-10). This suggests that processes associated with dimple formation and growth produce large numbers of event counts. Some other observations from this data include burst signals evident during crack growth by dimple coalescence and the apparent contradiction of the general trend of higher event counts with continuous signals from dimple growth. For example, the former observation is seen in comparing the results of the as-quenched, and quenched plus 400°C temper conditions. The latter observation is also seen in the results from the as-quenched condition. A recent model postulating the characteristics of acoustic emission from ductile crack growth [56] is not successful in explaining these conflicting observations. Added to this, the normalized plus 400°C temper exhibits a continuous signal during crack growth by cleavage (see Tables 5-8 and 5-10). Further detailed work to investigate these and other trends was prevented by external considerations, so further comments are not appropriate.

Some significant results were obtained with the amplitude distribution results. From a comparison of Tables 5-8 and 5-9, the following comments are made. The expansion of a plastic zone produces a two-part distribution similar in form and value of the exponent as that observed in the tensile tests. In these tests, continuous

signals are well represented by two-part amplitude distributions of the Weibull type as postulated by the theory in Chapter 4. For distributions observed in the loading range, P_{fmax} to P_Q, the distributions have two parts as shown in Figure 5.32. The distributions centered in the low amplitude have exponents similar in value to those observed during the testing of the as-received condition with a blunt notch. This suggests that these distributions are probably related to the expansion of plastic zone, regardless of heat treatment. The relation is not as conclusive as other sources of plastic deformation, because all tests include the shear lips and possibly plastic flow at the loading pins. The second distribution located at higher amplitudes in Figure 5.32 may be related to burst emissions of a moderately large amplitude. This is not unexpected and has been observed in tensile tests [28]. Again, no conclusive comments can be made without further detailed work being completed.

Where large to very large bursts were seen, the power law or straight line amplitude distribution is observed. Figure 5.33 is an example of this. The low amplitude distribution is from plastic deformation. The straight line distribution which extends to very high amplitudes usually has exponents in the range 0.3 to 1.0. There is no apparent separation of these types of distribution generated from cleavage or ductile crack growth.

In summary, the trends observed in the tensile test data were not always reflected in the compact tension test results. In fact, reversal of trends is not uncommon. For crack initiation and propagation, the AE properties observed in uniaxial tensile tests are not comparable.

The usual mechanical property relationships (e.g. K_Q to σ_{YS}) were not observed possibly in part because the tests were not carried out in plain strain.

6. CONCLUSIONS

Acoustic emission has been shown to be very strongly influenced by the variation in microstructure caused by heat treatment of A533B steel samples. The results from the series of tensile tests on normalized and tempered conditions have proven that the acoustic emission technique has revealed differences in dynamic deformation characteristics, which cannot be detected with the usual metallurgical /mechanical methods. This is another confirmation of the potential of acoustic emission as an investigative tool for materials research.

The observed trends of both the tempered martensite and bainite series have been correlated to a new model based on source characteristics, wave propagation and transducer behaviour. The relation of the source characteristics to microstructural terms was generally supported by the observed behaviour.

The correlation of acoustic emission to crack growth was less than conclusive. Obviously, further detailed work is required. The amplitude distribution analysis has been shown to reveal details of acoustic emission not evident in the RMS voltage signals. Present work has shown the capability of amplitude distribution to characterize deformation mechanisms, although more suitable methods of determining amplitude distribution functions other than by curve fitting, are desirable.

The lack of universal correlation between trends generated in the tensile and compact tension tests holds little promise for interpreting

acoustic emission data from large structures on the basis of simple laboratory tests.

REFERENCES

1. Gross, N.O. "Display and Analysis of Real Time Data from Acoustic Emission Tests of Pressure Vessels", Proceedings of 2nd Acoustic Emission Symposium, Sept. 1974, Tokyo, Japan, Tokyo, 1974, Sec. 1, pp. 1-65.

2. Spanner, J.C. "Acoustic Emission-Applications and Trends", Materials Engineering, Hanford Engineering Development Laboratory, Richland, Washington.

3. James, D.R. and S.H. Carpenter, "Relationship between Acoustic Emission and Dislocation Kinetics in Crystalline Solids", Journal of Applied Physics, Vol. 42, No. 12, pp. 4685-4697, November 1971.

4. Imanaka, T., K. Sano and M. Shimizu. "Dislocation Attenuation and Acoustic Emission during Deformation in Copper Single Crystals", Crystal Lattice Defects, Vol. 4, pp. 57-64, 1973.

5. Kuribayashi, K., et al. "The Fundamental Study of Acoustic Emission in the Plastic Deformation of Metals and Alloys", Proceedings of 3rd Acoustic Emission Symposium, Sept. 1976, Tokyo, Japan, JIPA, Tokyo, 1976, Sec. 4, pp. 271-287.

6. Kiesewetter, N. and P. Schiller. "The Acoustic Emission from Moving Dislocations in Aluminium", Phys. Stat. Sol. (a), Vol. 38, pp. 569-576, 1976.

7. Higgins, F.P. and S.H. Carpenter. "Sources of Acoustic Emission generated during the Tensile Deformation of Pure Iron", Acta Metallurgica, Vol. 26, pp. 133-139, 1978.

8. Siegel, E. "Burst Acoustic Emission during the Bauschinger Effect in F.C.C. and H.C.P. Metals and Alloys," Acta Metallurgica, Vol. 25, pp. 383-394, 1977.

9. Kishi, T., et al. "The Application of Acoustic Emission Technique to the study of Strain Hardening and Fatigue Hardening", Proceedings of the 3rd Acoustic Emission Symposium, Sept. 1976, Tokyo, Japan, JIPA, Tokyo, 1976, Sec. 4, pp. 305-325.

10. Frederick, J.R. and D.K. Felbeck. "Dislocation Motion as a Source of Acoustic Emission", Acoustic Emission, ASTM STP 505, American Society for Testing and Materials, 1972, pp. 129-139.

11. Achenbach, J.D. and J.G. Harris. "Acoustic Emission from a Brief Crack Propagation Event," to be published in Journal of Applied Mechanics.

12. Burridge, R. and J.R. Willis. "The self-similar problem of the expanding elliptical crack in an anisotropic solid," Proc. Camb. Phil. Soc., Vol. 66, pp. 443-468, 1969.

13. Freund, L.B. "The Initial Wave Front Emitted by a Suddenly Extending Crack in an Elastic Solid", Journal of Applied Mechanics, Vol. 39, pp. 601-602, June, 1972.

14. Pardee, W.J. "Acoustic Emission and the plate Green's function", Journal of Mathematical Physics, Vol. 18, No. 4, pp. 676-686, April,1977.

15. Stöckl, H. and F. Auer. "Dynamic Behaviour of a Tensile Crack: Finite Difference Simulation of Fracture Experiments", International Journal of Fracture, Vol. 12, No. 3, pp. 345-358, June, 1976.

16. Wadley, H.N.G. and C.B. Scruby. "A Study of Deformation and Fracture Processes in a Low Alloy Steel by Acoustic Emission Transient Analysis", United Kingdom Atom Energy Authority Harwell, Oxfordshire, AERE-R8913, October, 1977.

17. Pekeris, C.L. "The Seismic Surface Pulse", Proc. Natl. Acad. Sci., Vol. 41, pp. 469-480, 1955.

18. Pekeris, C.L. and Hanna Lifson. "Motion of the Surface of a Uniform Elastic Half-Space Produced by a Buried Pulse," Journal of the Acoustical Society of America, Vol. 29, No. 11, pp. 1233-1238, November, 1957.

19. Woodward, B. and R.W. Harris. "The Use of Signal Analysis to Identify Sources of Acoustic Emission, " Acustica, Vol. 37, pp. 190-197, 1977.

20. Graham, L.J. and G.A. Alers. "Spectrum Analysis of Acoustic Emission in A533-B Steel", Materials Evaluation, Vol. 32, No. 2, pp. 31-37, February, 1974.

21. Dunn, R.G., et al. "Molybdenum's Place in the Pressure Vessel Field", Climax Molybdenum Company, Connecticut, 1969, pp. 117.

22. Nippon Steel Company. "Low Alloy Plates for High Temperature Service", Cat. No. EXE 369, Tokyo, Japan, April, 1976.

23. Schmitt-Thomas, Kh.-G. "Acoustic emission measurements on an alloy of type Al CuMg2 with different hardening conditions", Aluminium, Vol. 51, No. 8, pp. 520-524, 1975.

24. Masuda, J. "The Acoustic Emission associated with the Deformation of Corson Alloys", Proceedings of the 4th Acoustic Emission Symposium, Sept. 1978, Tokyo, Japan, JIPA, Tokyo, 1978, Sec. 2, pp. 19-31.

25. Sano, K., et al. "Acoustic Emission during the Deformation of Tempered Martensitic Steel", Proceedings of the 2nd Acoustic Emission Symposium, Sept. 1974, Tokyo, Japan, JIPA, Tokyo, 1974, Sec. 5, pp. 23-45.

26. Hartbower, C.E., et al. "Monitoring Subcritical Crack Growth by Detection of Elastic Stress Waves", The Welding Journal, Research Supplement, Vol. 47, pp. 1s-18s, January, 1968.

27. Ono, K. "Acoustic Emission and Microscopic Deformation and Fracture Processes", Proceedings of 2nd Acoustic Emission Symposium, Sept. 1974, Japan, JIPA, Tokyo, 1974, Sec. 4., pp. 1-63.

28. Ono, K, R. Landy and C. Ouchi. "On the Amplitude Distribution of Burst Emission due to MnS Inclusions in HSLA Steels", Materials Dept.,School of Engineering and Applied Science, University of California, Los Angeles, Technical Report No. 78-03, July, 1978.

29. Ono, K. "Amplitude Distribution Analysis of Acoustic Emission Signals", Materials Evaluation, Vol. 34, No. 8, pp. 177-181, August, 1976.

30. Ono, K. and J. Statman. Unpublished work.

31. Pollock, A.A. "Acoustic Emission - A review of recent progress and technical aspects", Acoustics and Vibration Progress, Chapman and Hall, pp. 50-84.

32. Mogi, K. "Magnitude-Frequency Relation for Elastic Shocks Accompanying Fractures of Various Materials and Some Related Problems in Earthquakes", Bulletin of the Earthquake Research Institute, Vol. 40, pp. 831-853, 1962.

33. Evans, A.G. and M. Linzer. "Acoustic Emission in Brittle Materials", Am. Rev. Mater. Sci., Vol. 7, pp. 179-208, 1977.

34. Hatano, H. and K. Ono. "AE During Fracture Toughess Tests of A533B Steels", 16th Meeting of Acoustic Emission Working Group, Williamsburg, Virginia, October, 1976.

35. Ono, K., I. Roman and R. Landy. Unpublished work.

36. Lucia, A.C. and G. Redondi. "On the Interpretation of the Acoustic Emission Signals", Trans. ASME, Journal of Pressure Vessel Technology, Vol. 98J, No. 3, pp. 199-207, August, 1976.

37. Jax, P. and J. Eisenblatter. "Acoustic Emission Measurements During Plastic Deformation of Metals", Battelle Information, 15, pp. 2-8, 1972.

38. Kamfner, Y., et al. "Acoustic Emission Characteristics of Copper Alloys Under Low-Cycle Fatigue Conditions", Acoustic Emission Technology Corporation, Sacramento, California, Contract NAS3-18904 (NASA-CR-134766), April, 1975.

39. Enami, T., et al. "Effects of Cooling Rates and Tempering Conditions on Strength and Toughness of Mn-Ni-Mo, Cr-Mo Steel Plates", Kawasaki Steel Technical Report, Vol. 6, No. 2, pp. 15-31, April, 1974.

40. Speich, G. and W. Leslie. "Tempering of Steel", Metallurgical Transactions, Vol. 3, pp. 1043-1054, May, 1972.

41. Speich, G. "Tempering of Low C Martensite", Trans. of the Metallurgical Society of AIME, Vol. 245, pp. 2553-2564, December, 1969.

42. Henry, P. "The importance of Molybdenum in Heavy Steel Sections", Climax. Molybdenum, London.

43. Irvine, K.J. and F.B. Pickering. "The Tempering Characteristics of Low-Carbon Low-Alloy Steels", JISI, Vol. 194, pp. 137-153, February, 1960.

44. Anand, L. and J. Gurland. "The Relationship between the Size of Cementite Particles and the Subgrain Size in Quenched-and-Tempered Steels", Metallurgical Transactions, Vol. 6A, pp. 928-931, April, 1975.

45. Habraken, L.J. and M.Economopontos. "Bainitic Microstructures in Low-Carbon Alloy Steels and Their Mechanical Properties", Symposium, Climax Molybdenum, pp. 69-107, 1967.

46. Bush, M.E. and P.M. Kelly. "Strengthening Mechanisms in Bainitic Steels", Acta Metallurgica, Vol. 19, pp. 1363-1371, December, 1971.

47. Pickering, F.B. "The Structures and Properties of Bainite in Steels", Symposium, Climax Molybdenum, pp. 109-130, 1967.

48. Irvine, K.J., et al. "The Physical Metallurgy of Low-Carbon, Low-Alloy Steels Containing Boron", JISI, Vol. 186, pp. 56-67, 1957.

49. Irvine, K.J. and F.B. Pickering. "Low Carbon Bainitic Steels", JISI, Vol. 187, pp. 292-309, 1957.

50. Irvine, K.J. and F.B. Pickering. "The Metallography of Low-Carbon Bainitic Steels", JISI, Vol. 187, pp. 101-112, 1958.

51. Irvine, K.J. and F.B. Pickering. "The Impact Properties of Low-Carbon Bainitic Steels", JISI, Vol. 201, pp. 518-531, 1963.

52. Ohmori, Y., et al. "Tempering of the Bainite and the Bainite /Martensite Duplex Structure in a Low Carbon Low Alloy Steel", Metal Science, Vol. 8, pp. 357-366, 1974.

53. Ono, K. "Review of Recent Advances in Acoustic Emission Research", Proceedings of Fourth AE Symposium, Sept. 1978, Tokyo, Japan, JIPA, Tokyo, 1978, Sec. 7.

54. Malén, K. and L. Bolin. "A Theoretical Estimate of Acoustic-Emission Stress Amplitudes", Phys. stat. sol. (b), Vol. 61, pp. 637-645, 1974.

55. Takeuchi, T. "The Effect of Strain Rate Change on the Flow Stress of Iron Single Crystals", Proceedings of the ICSTIS, pp. 1229-1232, Sec. 6, Suppl. Trans. ISIJ, Vol. 11, 1971.

56. Sano, K. and K. Fujimoto. "Microscopic Aspects of Fracture and Acoustic Emission in Metals", Research Laboratories, Kawasaki Steel Corporation, 1978.

Tables and Figures

TABLE 1-1

TYPICAL COOLING RATES FOR PLATES OF VARIOUS THICKNESSES

Thickness inch	TYPE OF HEAT TREATMENT					
	Dip Quench			Normalize		
	1/4 T	1/2 T	Ratio	1/4 T	1/2 T	Ratio
2	NA	1×10^3	-	NA	1×10^3	-
4	1×10^4	5×10^2	0.02	7×10^3	4×10^2	0.06
6	4×10^3	3×10^2	0.08	2×10^3	1×10^2	0.10
8	3×10^3	NA	-	1×10^3	NA	-

Units of cooling rate in °C/hr.
NA = not available

TABLE 3-1

CHEMICAL COMPOSITION OF A533B Cℓ 2 STEEL

C	Si	Mn	P	S	Cu	Ni	Cr	Mo
0.20	0.23	1.43	0.007	0.004	0.03	0.60	0.10	0.53
As	Sn	Sb	Co	Aℓ	B	H	N	V
0.007	0.005	0.001	0.018	0.024	0.0005	0.00019	0.0063	0.006

TABLE 3-2

HEAT TREATMENT SCHEDULE

Heat Treatment	Specimen	Heat Treatment	Specimen
N-normalized	T, CT	Q-quenched	T, CT
N + 100°C Temper 24 hours	T	Q + 100°C Temper 24 hours	T
N + 200	T	Q + 200	T
N + 300	T	Q + 300	T
N + 400	T, CT	Q + 400	T, CT
N + 500	T	Q + 500	T
N + 600	T	Q + 600	T
N + 650	T	Q + 650	T
N + 700	T, CT	Q + 700	T, CT
N + 750	T	Q + 750	T
Full anneal 930°C 1 hour FC	T, CT	930°C 1 hour → isothermal 650°C 24 hours	T
As-received	T, CT		
As + 700°C	T		
As + 650°C	T		

T = tensile
CT = compact tension

TABLE 5-1

MECHANICAL AND ACOUSTIC EMISSION PROPERTIES OF

TEMPERED AS-RECEIVED STEEL

Properties	Heat Treatment		
	As-received (transverse drn)	As-received (thickness drn)	As-received + 650°C
σ_{YS} MPa	511.45	437.77	396.45
(ksi)	(74.18)	(63.64)	(57.50)
σ_{UTS} MPa	711.93	573.77	523.88
(ksi)	(103.26)	(83.22)	(75.98)
RA %	67	61	67
V_r^P μV	17.2	57.0	9.9
σ_P MPa	469.96	439.12	396.75
(ksi)	(68.17)	(63.64)	(57.50)
σ_{AE} MPa	55.29	81.08	28.36
(ksi)	(8.02)	(11.75)	(4.11)
σ_B MPa	82.93	81.08	410.90
(ksi)	(12.03)	(11.75)	(59.55)
N_e TOTAL X1,000	99.2*	32.6	1.5*
N_e YIELD X1,000	16.0*	5.6	0.5*
$\overline{V}_r$ TOTAL	12.0	9.28	2.60
YIELD ($X10^{-4}$ Vsec)	7.25	2.64	0.38
$\overline{V}_r^2$ TOTAL	13.3	18.8	0.97
YIELD ($X10^{-9}$ V^2sec)	11.4	8.31	0.06

* estimates from tape replay

TABLE 5-2

MECHANICAL AND ACOUSTIC EMISSION PROPERTIES OF

MISCELLANEOUS HEAT TREATMENTS

Properties	HEAT TREATMENT		
	As-received + 700°C	Full Anneal	Isothermally Transformed at 650°C
σ_{YS} MPa	264.96	576.29	343.07
(ksi)	(38.40)	(83.52)	(49.72)
σ_{UTS} MPa	603.82	754.86	528.40
(ksi)	(87.51)	(109.40)	(76.58)
RA %	57	65	58
V_r^P μV	14.7	7.4	30.0
σ_P MPa	223.08	477.89	349.97
(ksi)	(32.33)	(69.26)	(50.72)
σ_{AE} MPa	41.81	56.24	82.32
(ksi)	(6.06)	(8.15)	(11.93)
σ_B MPa	55.75	140.55	150.97
(ksi)	(8.08)	(20.37)	(21.88)
N_e TOTAL X1000	119.8	96.0*	140.4
N_e YIELD X1000	27.0	48.0*	39.4
$\overline{V}_r$ TOTAL	7.65	3.01	6.90
YIELD	2.20	1.96	1.14
($X10^{-4}$Vsec)			
$\overline{V}_r^2$ TOTAL	5.41	9.77	6.98
YIELD	2.63	9.60	1.76
($X10^{-9}$ V^2sec)			

* estimates from tape replay

TABLE 5-3

AMPLITUDE DISTRIBUTION EXPONENTS, m, FROM TENSILE

TESTS OF QUENCHED AND TEMPERED STEELS

Heat Treatment	EXPONENTS		
	Preyield	Yield	Initial Work Hardening
As-quenched	2.5	4 + 1	
Q + 100°C	4 + 1	4	4
Q + 200°C	3*	4 + 1	3
Q + 300°C	4	4 + 2, 4	4, 3
Q + 400°C	1.5 → 1	4, 3	4 + 1
Q + 500°C	1.25*	4	4 + 1, 4
Q + 600°C	1.5*	4	
Q + 650°C	3 → 4	4 + 3	3
Q + 700°C		4, 4	4
Q + 750°C	4	4	4

* denotes the experimental curve is better fitted by a straight line or power law

A + B indicates amplitude distribution can be separated into two components

TABLE 5-4

INITIAL DISTRIBUTION EXPONENTS, m, FROM TENSILE

TESTS OF NORMALIZED AND TEMPERED STEELS

Heat Treatment	EXPONENTS		
	Preyield	Yield	Initial Work Hardening
Normalized		4	4 + 0.5
N + 100°C	4	4, 4	4, 4
N + 200°C	4	4	4 + 0.5
N + 300°C	4	2, 4	4
N + 400°C*	1	1, 2	4 + 0.5
N + 500°C*		1	
N + 600°C	1.5**	1.5	1.5 + 0.5
N + 650°C*		2	1
N + 700°C*	2	2, 4	4
N + 750°C	4	4, 4	4 + 0.5

*recorded by a broad band transducer

**denotes experimental curve better fitted by a straight line or power law

A + B indicates amplitude distribution can be separated into two components

TABLE 5-5

AMPLITUDE DISTRIBUTION EXPONENTS, m, FROM

TENSILE TESTS OF MISCELLANEOUS HEAT TREATMENT

Heat Treatment	EXPONENTS		
	Preyield	Yield	Initial Work Hardening
As-received* (transverse drn)	1	2	0.4
As-received (thickness drn)	0.5	4 + 0.5; 4 + 0.4	0.5
As-received* + 650°C		1	0.35
As-received* + 700°C		4	4; 0.3→0.4
Full Anneal*		2	
Isothermally* transformed at 650°C	1	1	0.5

* recorded by a broad band transducer

A + B = indicates amplitude distribution can be separated into two components.

TABLE 5-6

ACOUSTIC EMISSION DURING NECKING IN THE TENSILE TESTS

Heat Treatment	n_y	Remarks
N	0.75	None; none
N + 100	0.77	Some continuous signal
N + 200	0.72	Considerable burst; none; none.
N + 300	0.76	Few burst
N + 400	0.79	Few burst; few burst
N + 500	0.80	Considerable burst; none
N + 600	0.81	Some continuous signal
N + 650	0.79	None; none
N + 700	0.55	Small continuous signal; none
N + 750	0.64	None
Q	0.75	Considerable burst; some burst; none
Q + 100	0.78	None
Q + 200	0.81	Some continuous signal
Q + 300	0.88	None
Q + 400	0.93	None
Q + 500	0.92	None
Q + 600	0.89	None; none
Q + 650	0.86	Some small continuous signals; none
Q + 700	0.51	Some continuous signal from all three tests
Q + 750	0.70	Some continuous signal; none
As-received	0.72	Few bursts; none
As-received + 650	0.76	Few bursts; none
As-received + 700	0.44	None from all tests
Full anneal	0.74	None from all tests
Isothermal transformed at 650°C	0.60	None from all tests
As-received (Z drn)	0.76	Burst emission; none

N = Normalized
Q = Quenched

TABLE 5-7

MECHANICAL AND ACOUSTIC EMISSION PROPERTIES FROM THE COMPACT TENSION TESTS

Heat Treatment	P_{fmax} kN (kip)	P_Q kN (kip)	P_{max} kN (kip)	K_Q $MN \cdot m^{-3/2}$ ($ksi\sqrt{in}$)	$N_e(P_Q)$ X1000	$N_e(P_{max})$ X1000	σ_{YS} MPa (ksi)
As-received		29.47	83.40	61.16	38.0	280.0	524
(blunt notch)		(6.63)	(18.75)	(55.60)			(76)
As-received	6.67	20.02	33.58	54.34	7.3	12.0	524
	(1.50)	(4.50)	(7.55)	(49.40)			(76)
Normalized	13.34	24.46	26.69	61.42	29.2	44.0	607
	(3.00)	(5.50)	(6.00)	(55.84)			(88)
Normalized + 400°C	13.34 (3.00)	18.24 (4.10)	28.02 (6.30)	75.79 (68.90)	8.2	106.0	607 (88)
Normalized + 700°C	13.34 (3.00)	21.05 (4.50)	31.69 (7.13)	55.00 (50.00)	1.9	63.7	352 (51)
As-Quenched	13.34	33.80	51.15	99.99	0.6	2.8	1173
	(3.00)	(7.60)	(11.50)	(90.90)			(170)
Quenched + 400°C	13.34 (3.00)	50.04 (11.25)	57.82 (13.00)	133.65 (121.50)	72.0	108.4	1076 (156)
Quenched + 700°C	13.34 (3.00)	25.35 (5.70)	39.14 (8.80)	68.09 (61.90)	3.9	51.6	380 (55)
Full Anneal	8.90	42.78	52.26	64.13	32.00	158.0	566
	(2.00)	(6.20)	(11.75)	(58.30)			(82)

TABLE 5-8

THE CHARACTERISTICS OF AE SIGNALS FROM THE COMPACT TENSION TESTS

Heat Treatment	LOAD RANGE			
	$0 \rightarrow P_{fmax}$	$P_{fmax} \rightarrow P_Q$	$P_Q \rightarrow P_{max}$	$P_{max} \rightarrow$ end
As-received (blunt notch)	B	C	B + C	
As-received	B	B	B	B
Normalized	B	B + C	C + few B	B
Normalized + 400°C	B	C	C	B
Normalized + 700°C	B	B + C	Large B+C	B
As-quenched	B	B	Very large B	Very large B
Quenched + 400°C	B	C+few B	Large B + C	B
Quenched + 700°C	B	B + C	B + C	B
Full Anneal	B	B + C	B + C	B + C

B = burst type AE

C = continuous type AE

TABLE 5-9

AMPLITUDE DISTRIBUTION EXPONENTS, m, FROM THE COMPACT TENSION TESTS

Heat Treatment	LOAD RANGE			
	$0 \rightarrow P_{fmax}$	$P_{fmax} \rightarrow P_Q$	$P_Q \rightarrow P_{max}$	$P_{max} \rightarrow$ end
As-received (blunt notch)	4 + 0.3	2 + 0.9*	4 + 0.3	4
As-received	4 + 0.3	4 + 0.3	4 + 0.47*	4 + 0.3
Normalized	4+0.5→0.3	4 + 0.3*	4 + 0.4*	4 + 0.4*
Normalized + 400°C	2	4+1; 4+1	4 + 1	2
Normalized + 700°C	4 + 0.3	2+0.35→0.5	4 + 0.33*	4 + 0.3
As-quenched	4+0.70*→ 0.90*	4 + 0.5*	4 + 0.4*	4 + 0.47*
Quenched + 400°C	4 + 0.3→ 0.5	4 + 1.44*	4 + 0.50 4 + 2.2*	4 + 0.233* 4 + 0.2*
Quenched + 700°C	4 + 1.13*	4; 2+1.0* 2+0.78*	4 + 0.74*	4 + 0.93*
Full Anneal	4 + 0.3	4 + 0.3	2 + 0.35	2 + 0.89*

* indicates experimental curve better fitted by straight line or power law.

A+B denotes amplitude distribution can be separated into two components.

TABLE 5-10

FRACTURE SURFACE CHARACTERISTIC OF HEAT TREATED COMPACT TENSION SAMPLES

Heat Treatment	Initiation	Propagation	Remarks
As-received (blunt notch)	thumbnail shaped area of very large dimples	cleavage outside this thumbnail shaped dimple formation	shear lip and lateral contraction at crack tip.
As-received	stretch zone (sz)	cleavage	small shear lip and slight lateral contraction
Normalized	cleavage starts at boundary of sz	cleavage	small shear lip
Normalized + 400°C	sz mixture of large and small equiaxed dimples	cleavage	small shear lip
Normalized + 700°C	dimples in a very small sz	cleavage	shear lip and lateral contraction
As-quenched	sz observed to merge with dimples	large dimples	very large shear lips
Quenched + 400°C	elongated dimples in a small sz	elongated dimples	very large shear lips
Quenched + 700°C	sz indistinguishable from dimples	equiaxed dimples	considerable lateral contraction and very small shear lip
Full Anneal	elongated dimples in sz	cleavage	shear lip and lateral contraction

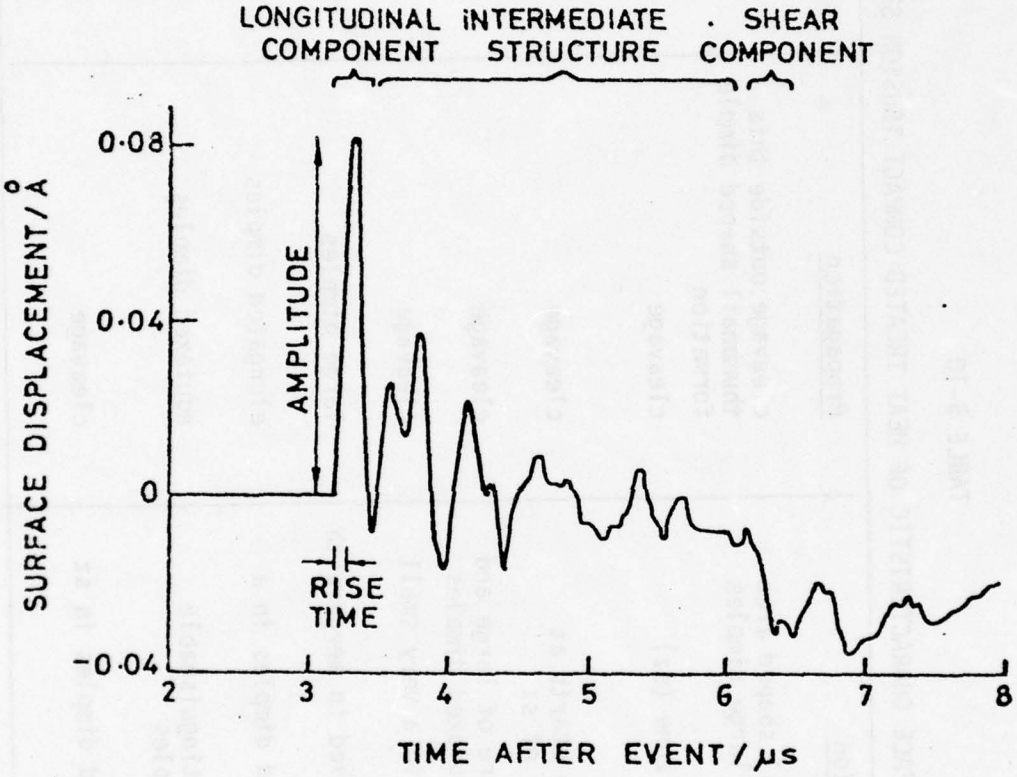

FIGURE 1.1 A typical transient measured with a calibrated broad band system.

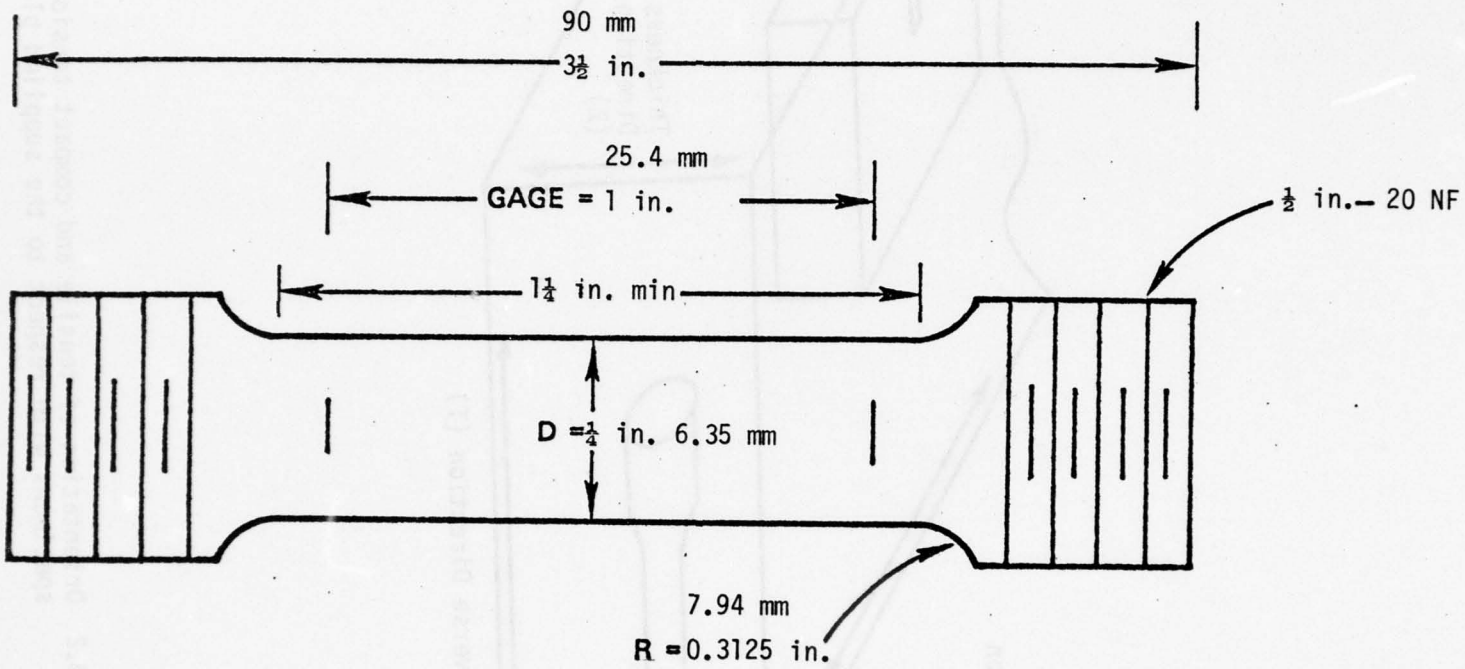

FIGURE 3.1 Dimensions of tensile specimens.

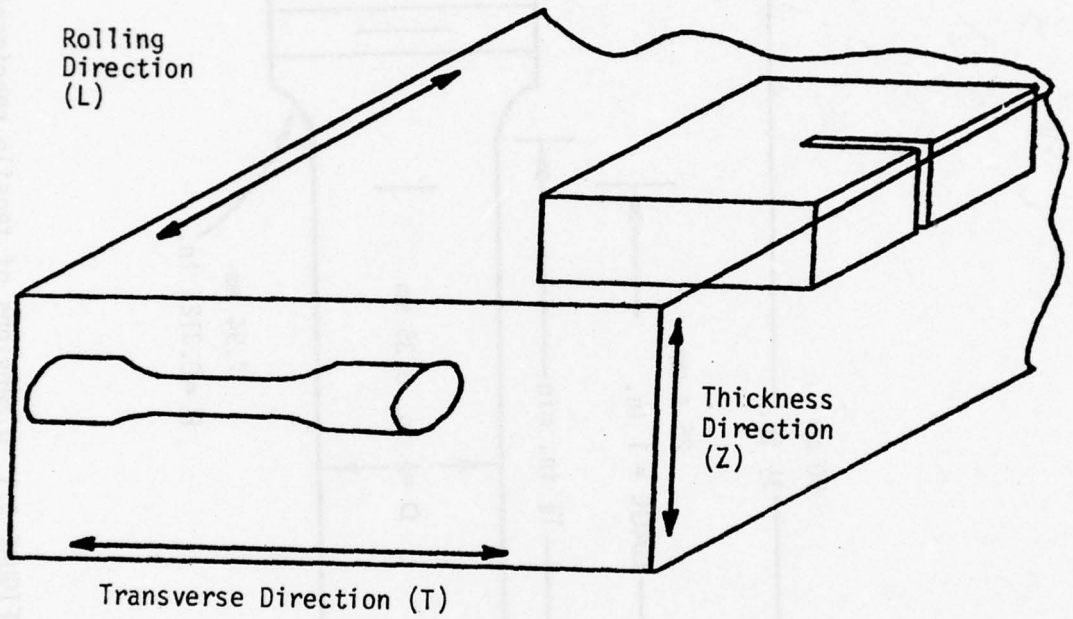

FIGURE 3.2 Orientation of tensile and compact tension specimens with respect to the supplied plate.

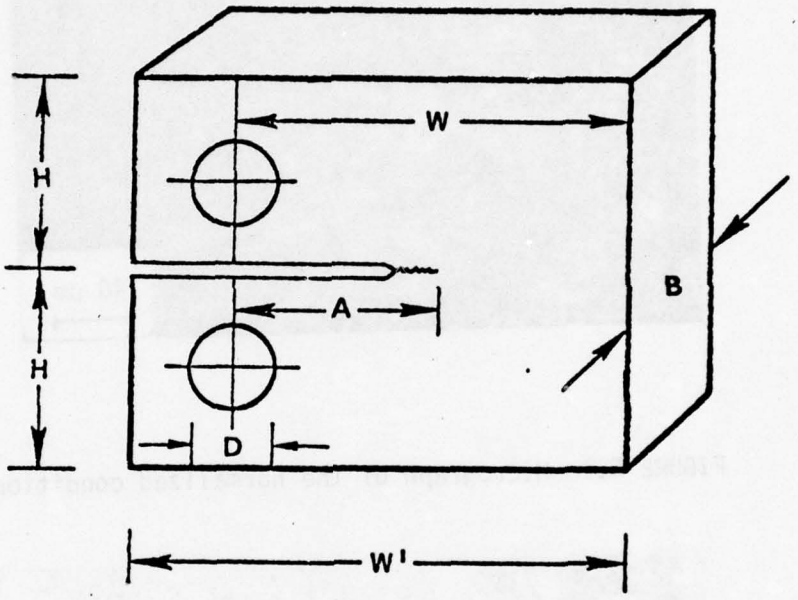

B = 0.75 in (19 mm)
W = 1.50 in (38 mm)
H = 0.90 in (23 mm)
D = 0.375 in (10 mm)
W' = 1.875 in (48 mm)

FIGURE 3.3 Dimensions of compact tension specimens.

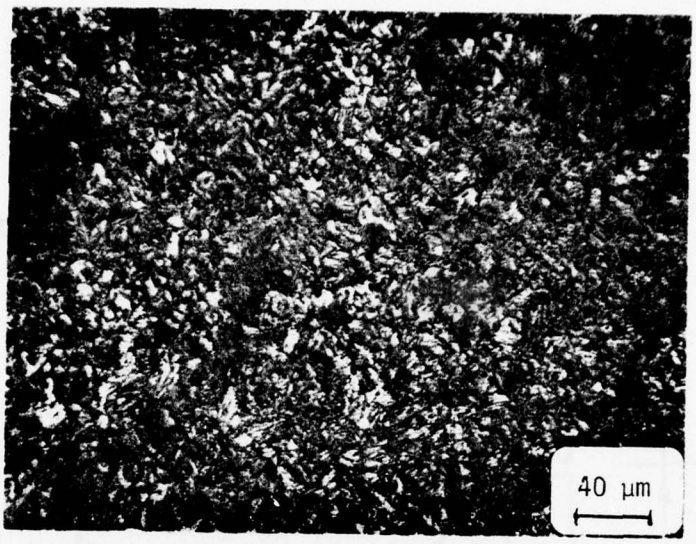

FIGURE 5.1 Micrograph of the normalized condition.

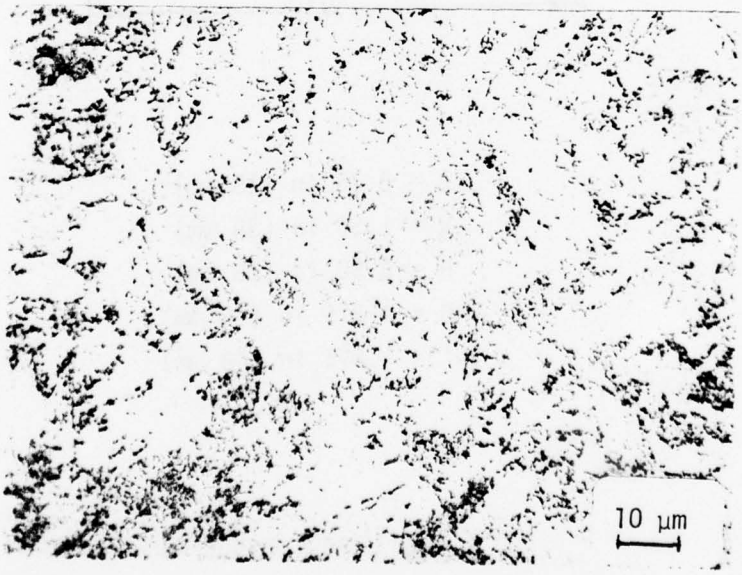

FIGURE 5.2 Micrograph of the as-received condition.

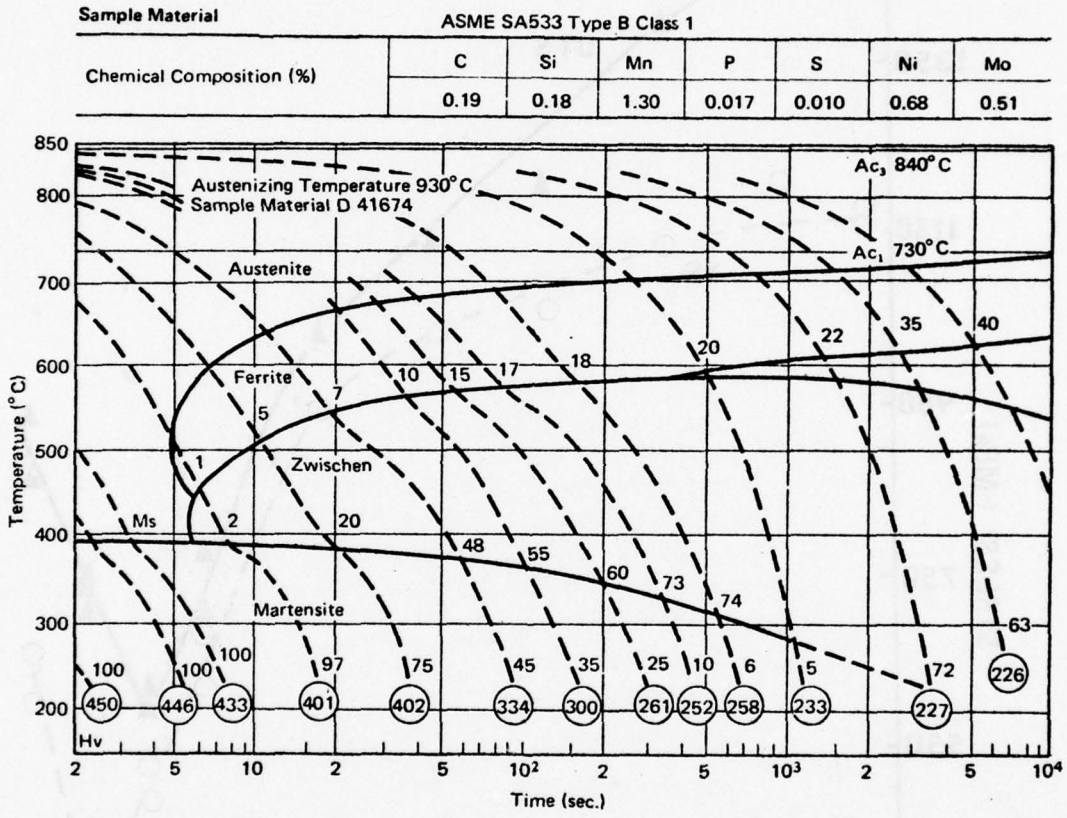

FIGURE 5.3 Continuous-cooling-transformation diagram for A533B steel.

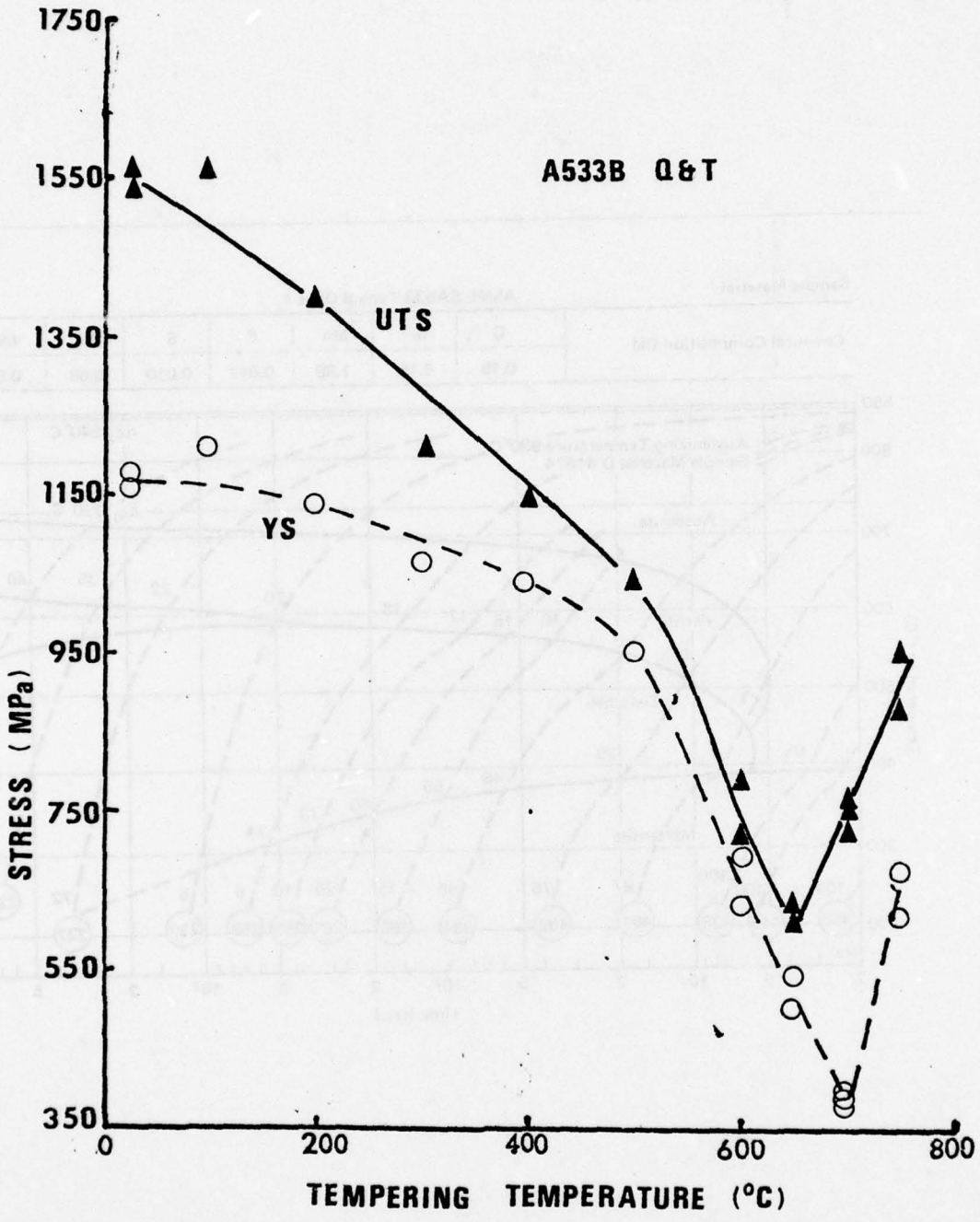

FIGURE 5.4 Tensile properties of martensitic A533B steel as a function of tempering temperature.

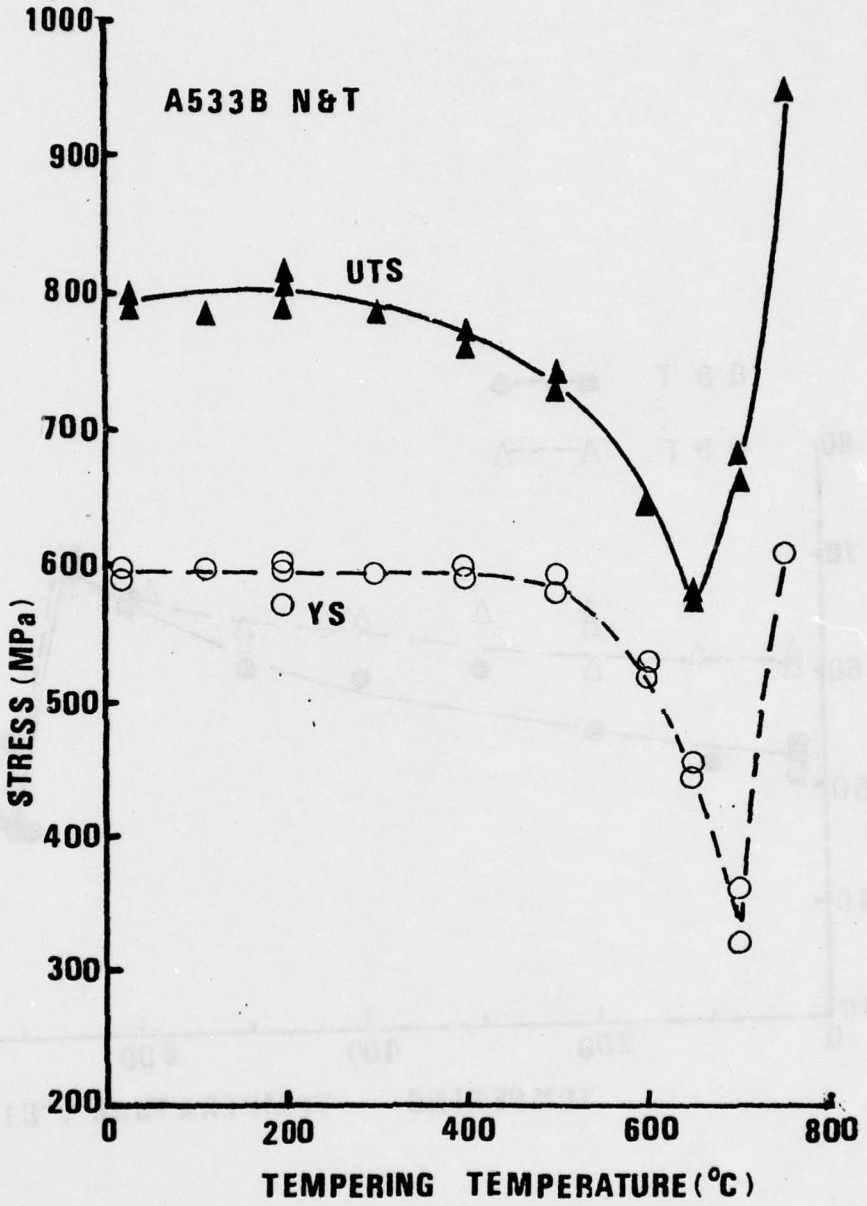

FIGURE 5.5 Tensile properties of bainitic A533B steel as a function of tempering temperature.

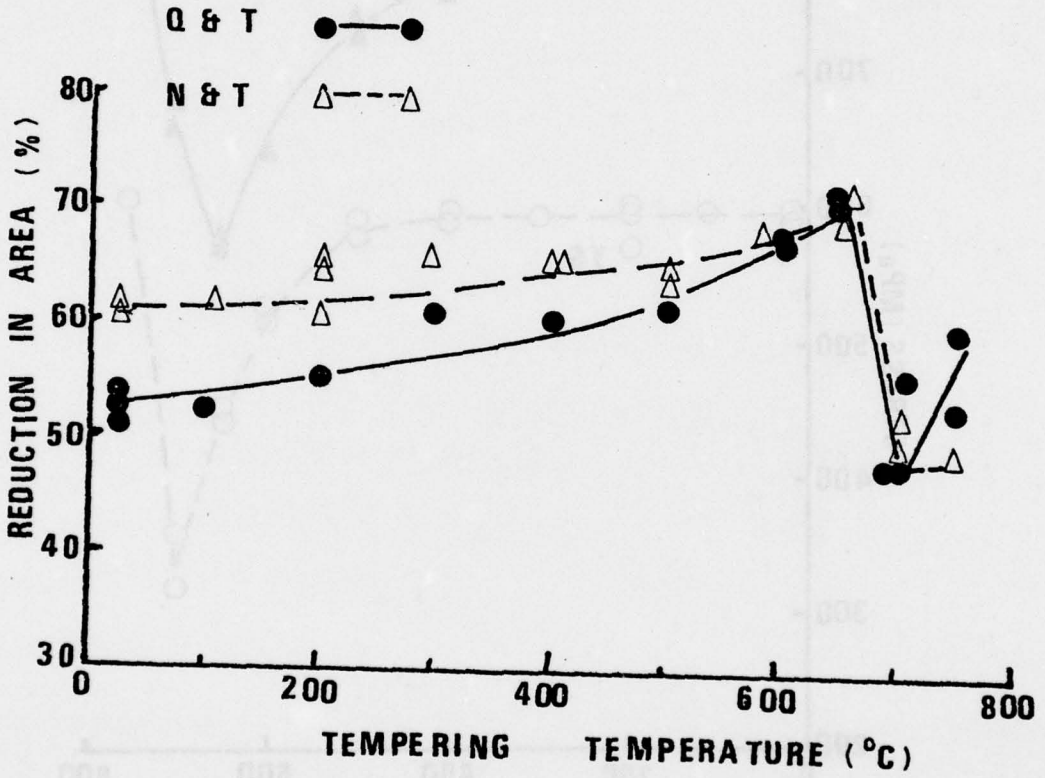

FIGURE 5.6 The reduction in area at fracture for normalized and quenched A533B steel as a function of tempering temperature.

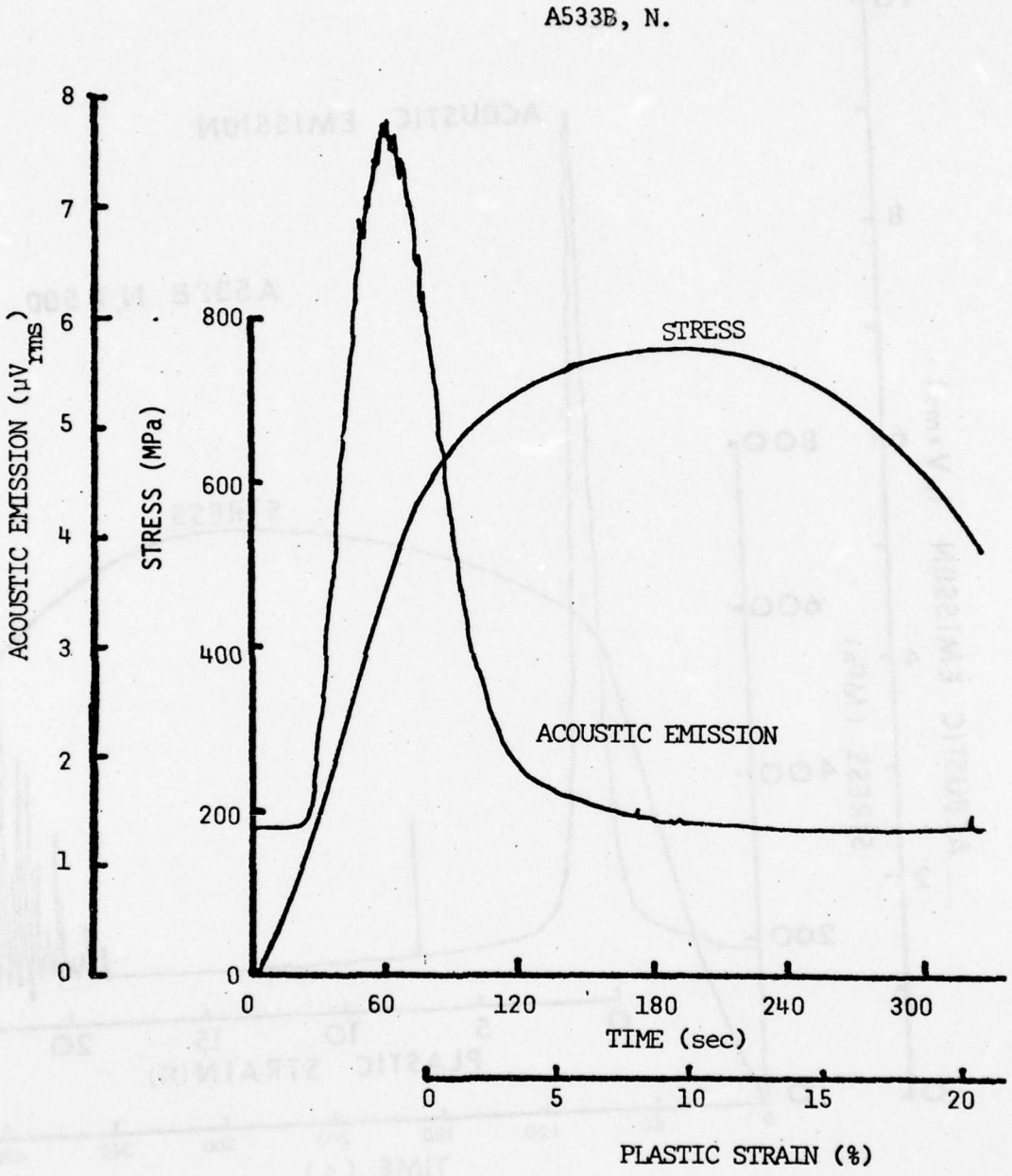

FIGURE 5.7 AE RMS voltage and stress against time for normalized A533B steel.

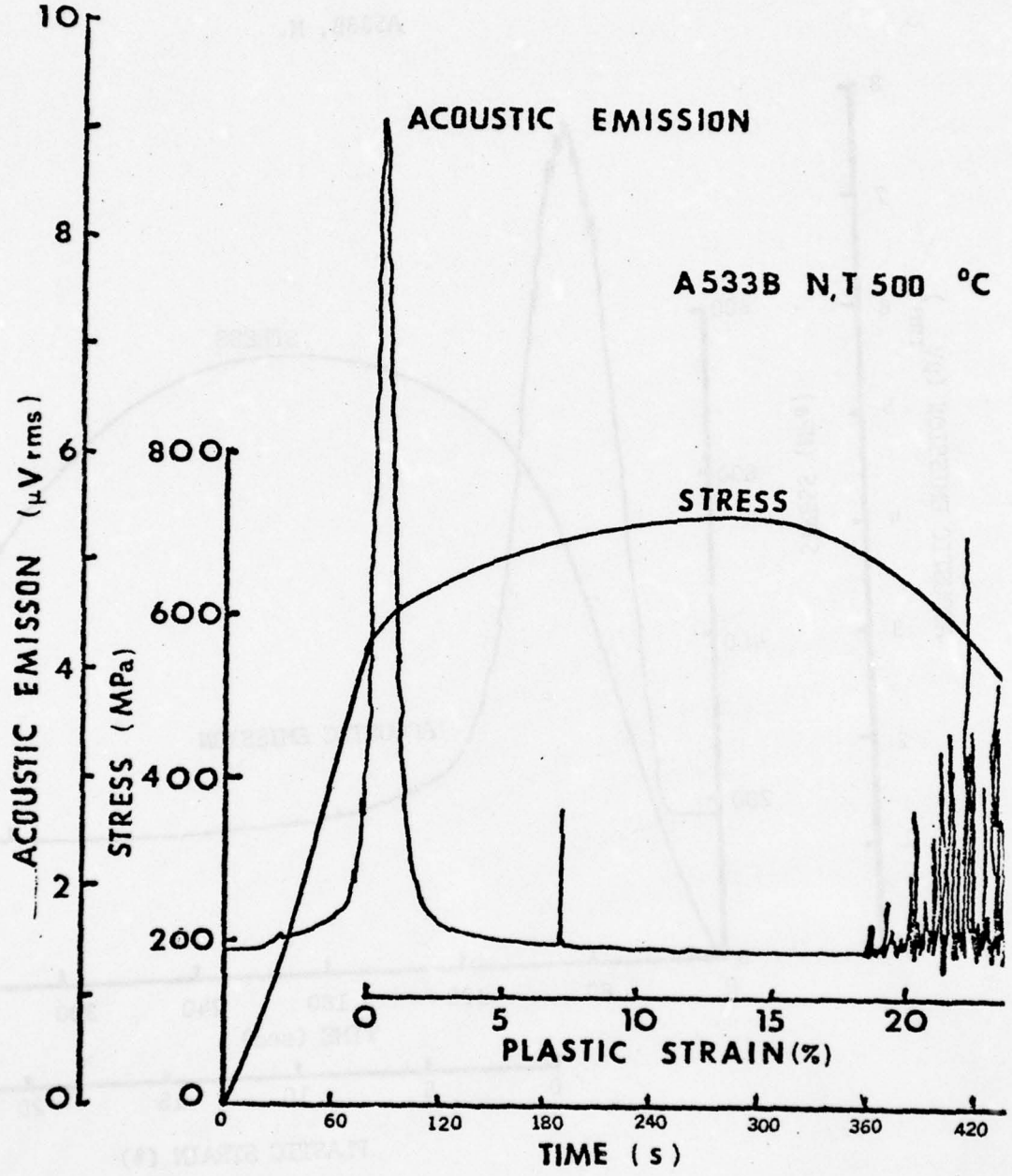

FIGURE 5.8 AE RMS voltage and stress against time for the normalized plus 500°C temper condition of A533B steel.

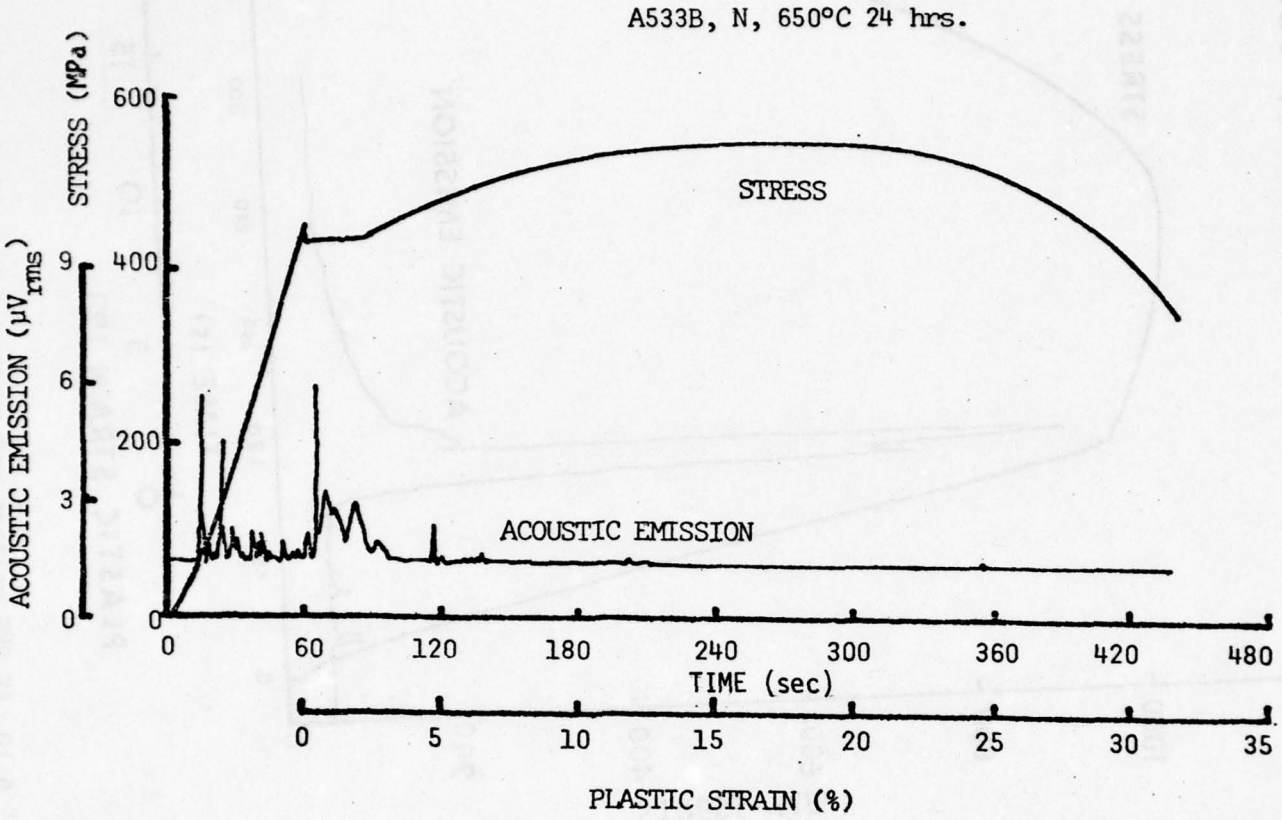

FIGURE 5.9 AE RMS voltage and stress against time for the normalized plus 650°C temper condition of A533B steel.

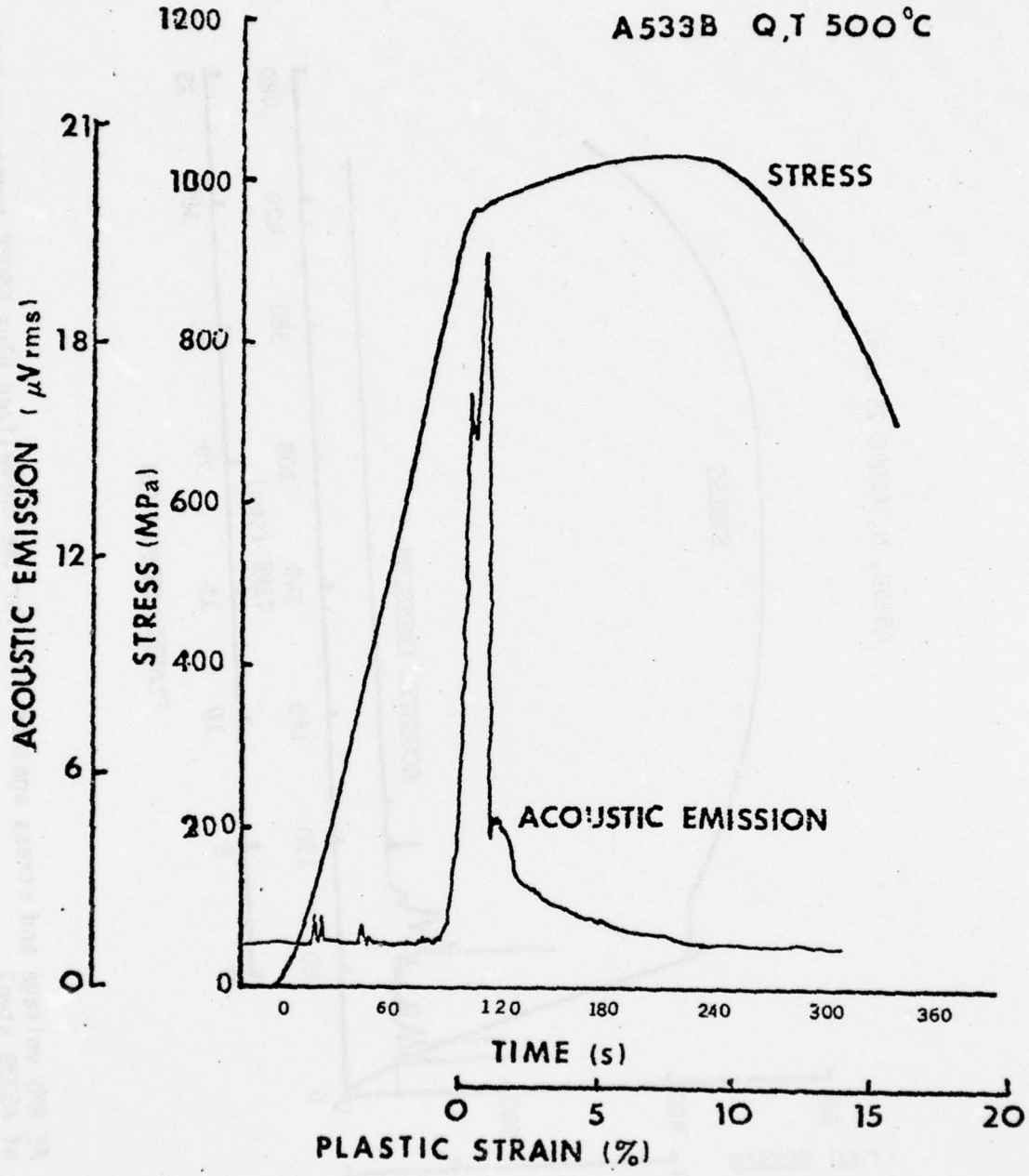

FIGURE 5.10 AE RMS voltage and stress against time for the quenched plus 500°C temper condition of A533B steel.

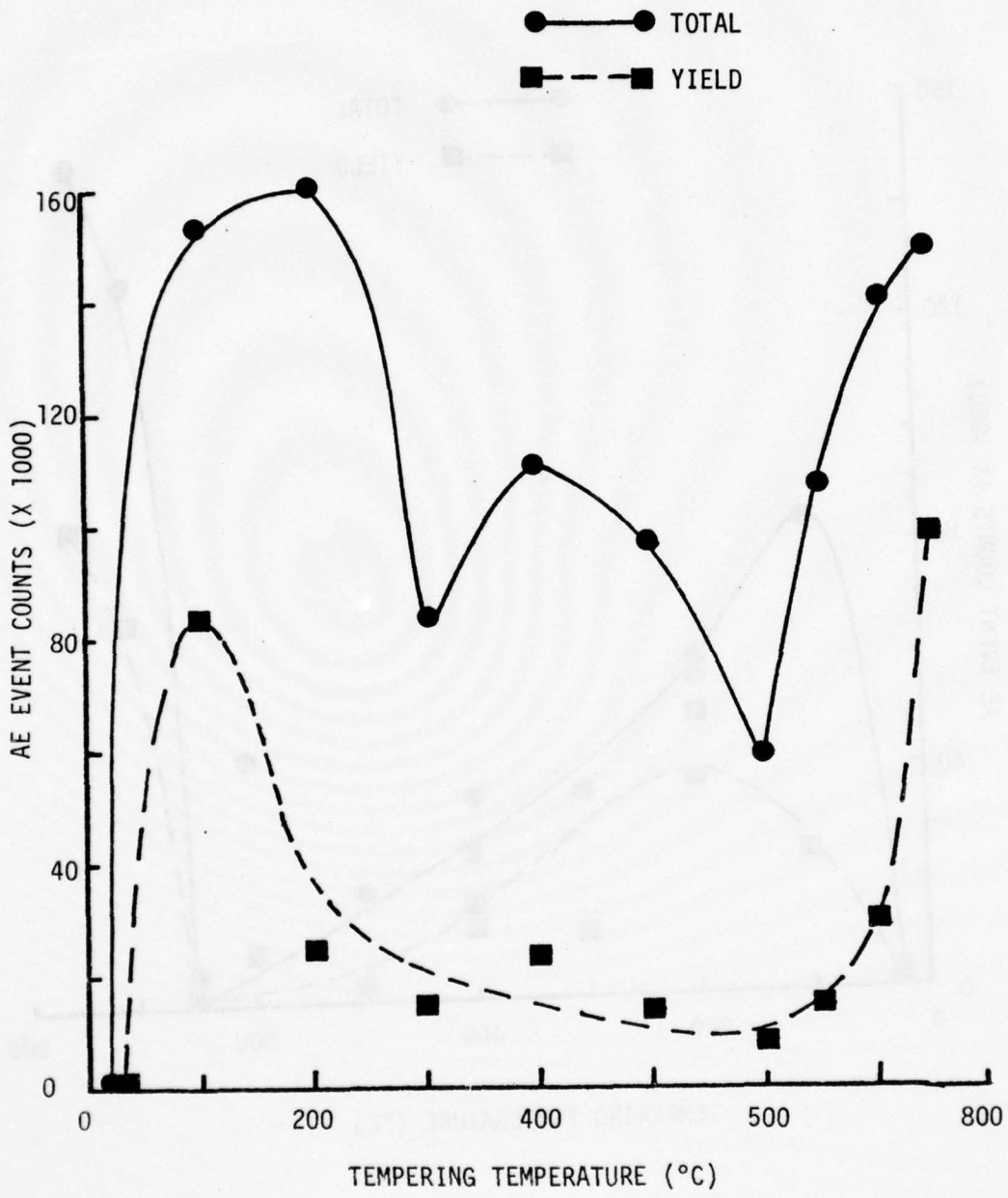

FIGURE 5.11 AE Event Counts for martensitic steel as a function of tempering temperature.

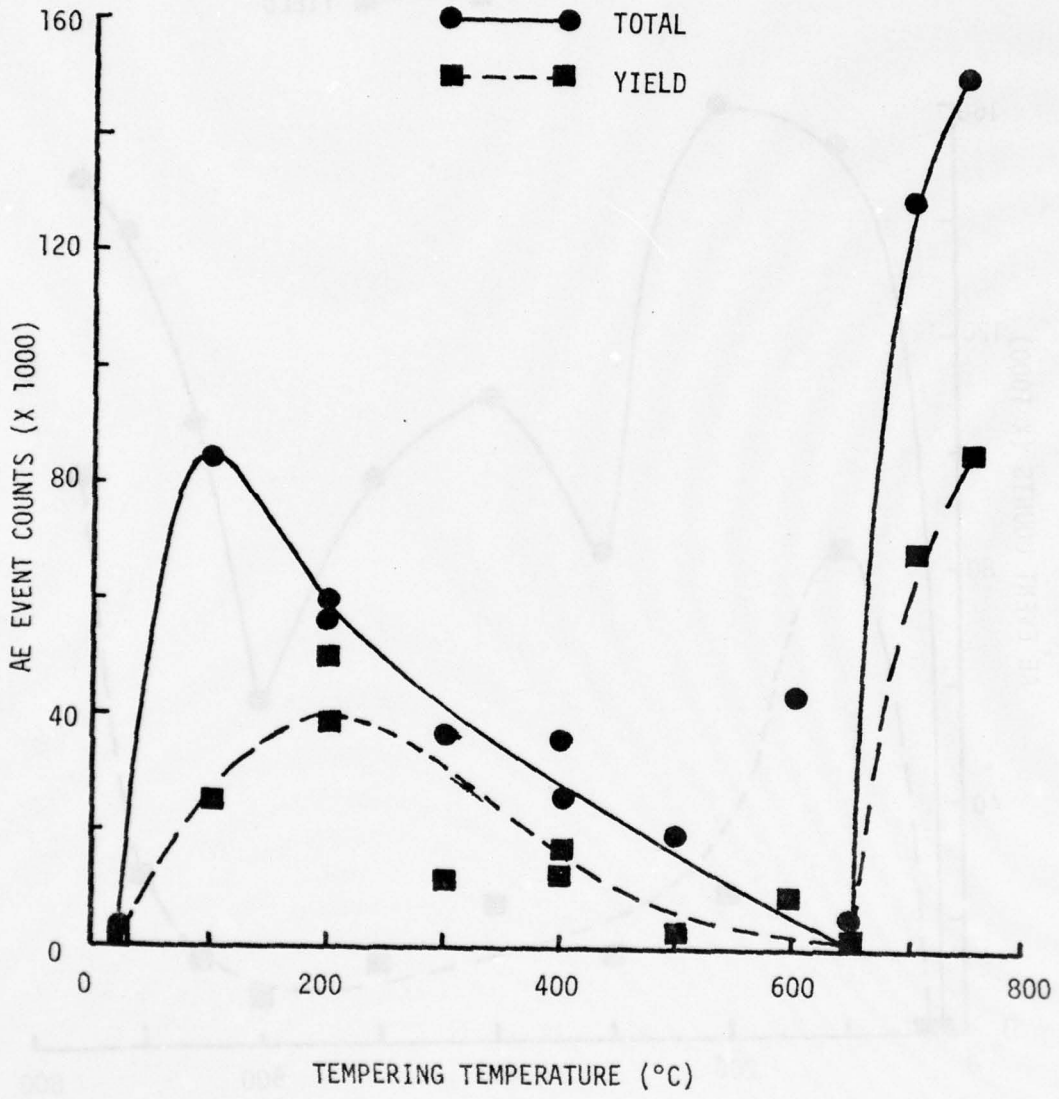

FIGURE 5.12 AE Event Counts for bainitic steel as a function of tempering temperature.

AD-A069 965 CALIFORNIA UNIV LOS ANGELES DEPT OF MATERIALS F/G 11/6
ACOUSTIC EMISSION BEHAVIOUR OF A LOW ALLOY STEEL.(U)
MAY 79 R J LANDY N00014-75-C-0419
UNCLASSIFIED TR-79-02 NL

2 OF 2
AD A069965

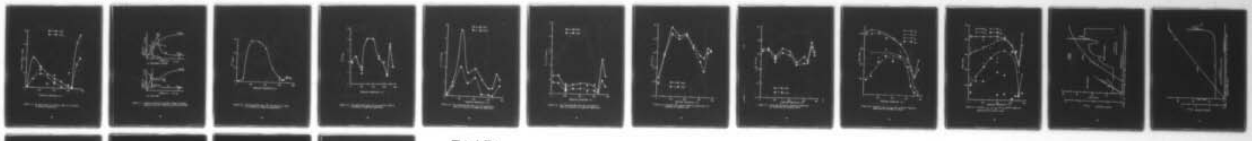

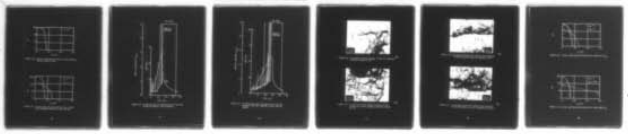

END
DATE FILMED
7-79
DDC

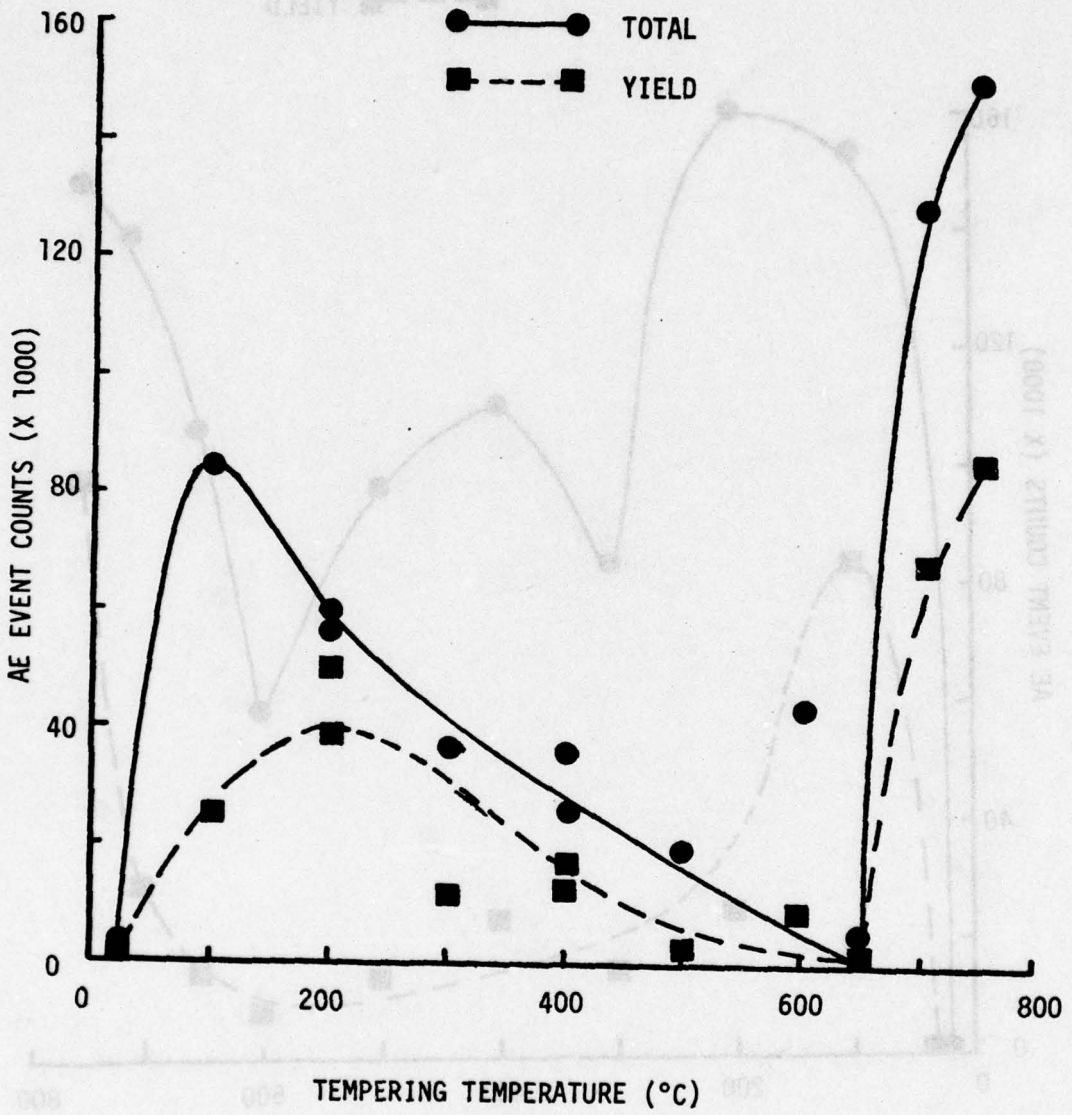

FIGURE 5.12 AE Event Counts for bainitic steel as a function of tempering temperature.

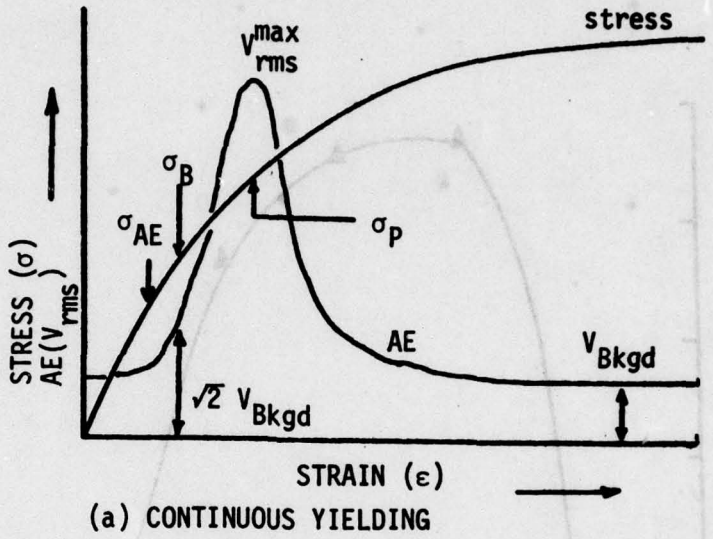

(a) CONTINUOUS YIELDING

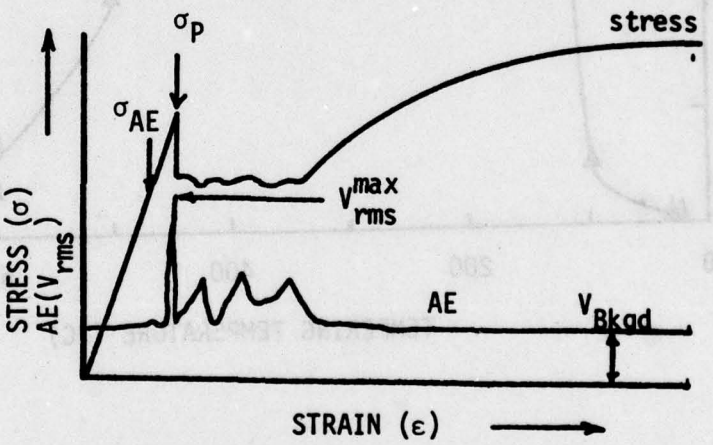

(b) YIELD DROP

FIGURE 5.13 Schematic drawings of AE RMS voltage and stress against strain for different yielding conditions.

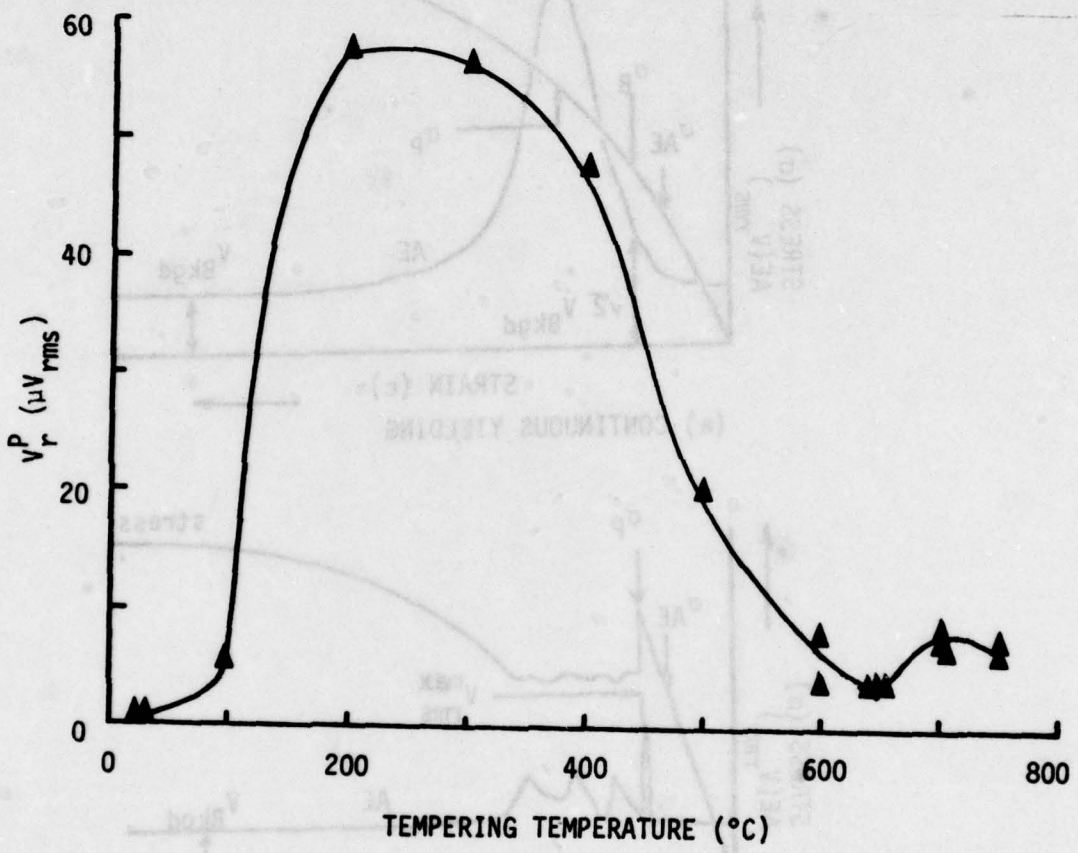

FIGURE 5.14 The maximum RMS level, V_r^P, for martensitic steel as a function of tempering temperature.

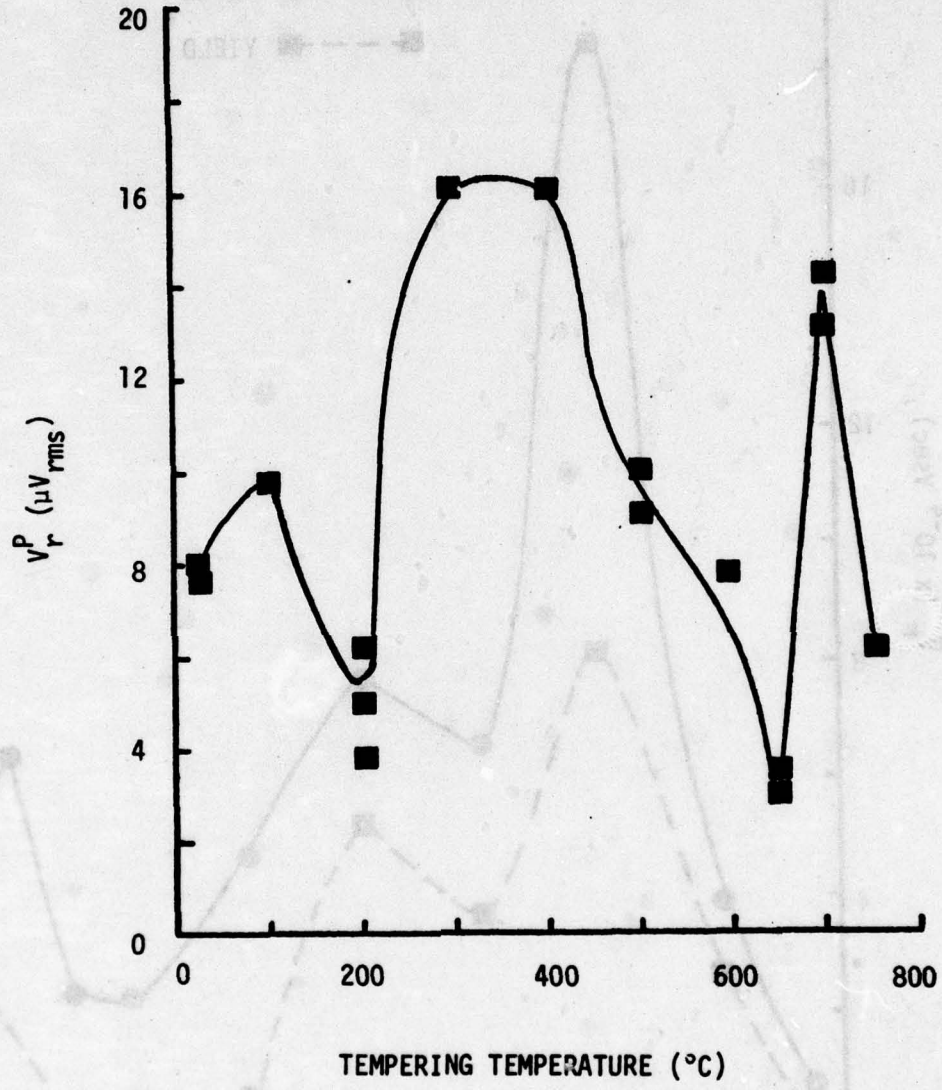

FIGURE 5.15 The maximum RMS level, V_r^P, for bainitic steel as a function of tempering temperature.

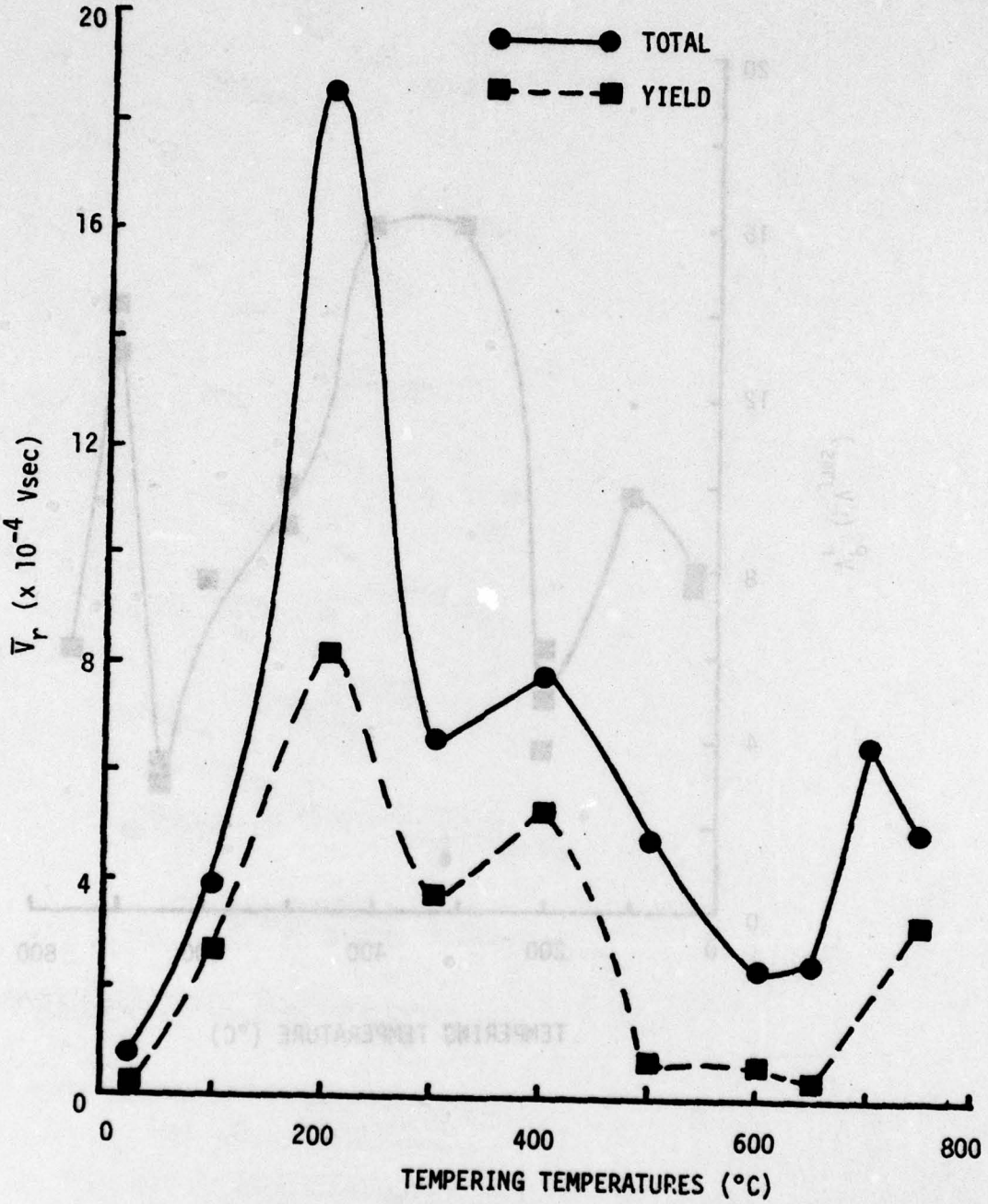

FIGURE 5.16 The integrated RMS level, $\bar{V}_r$, for martensitic steel as a function of tempering temperature.

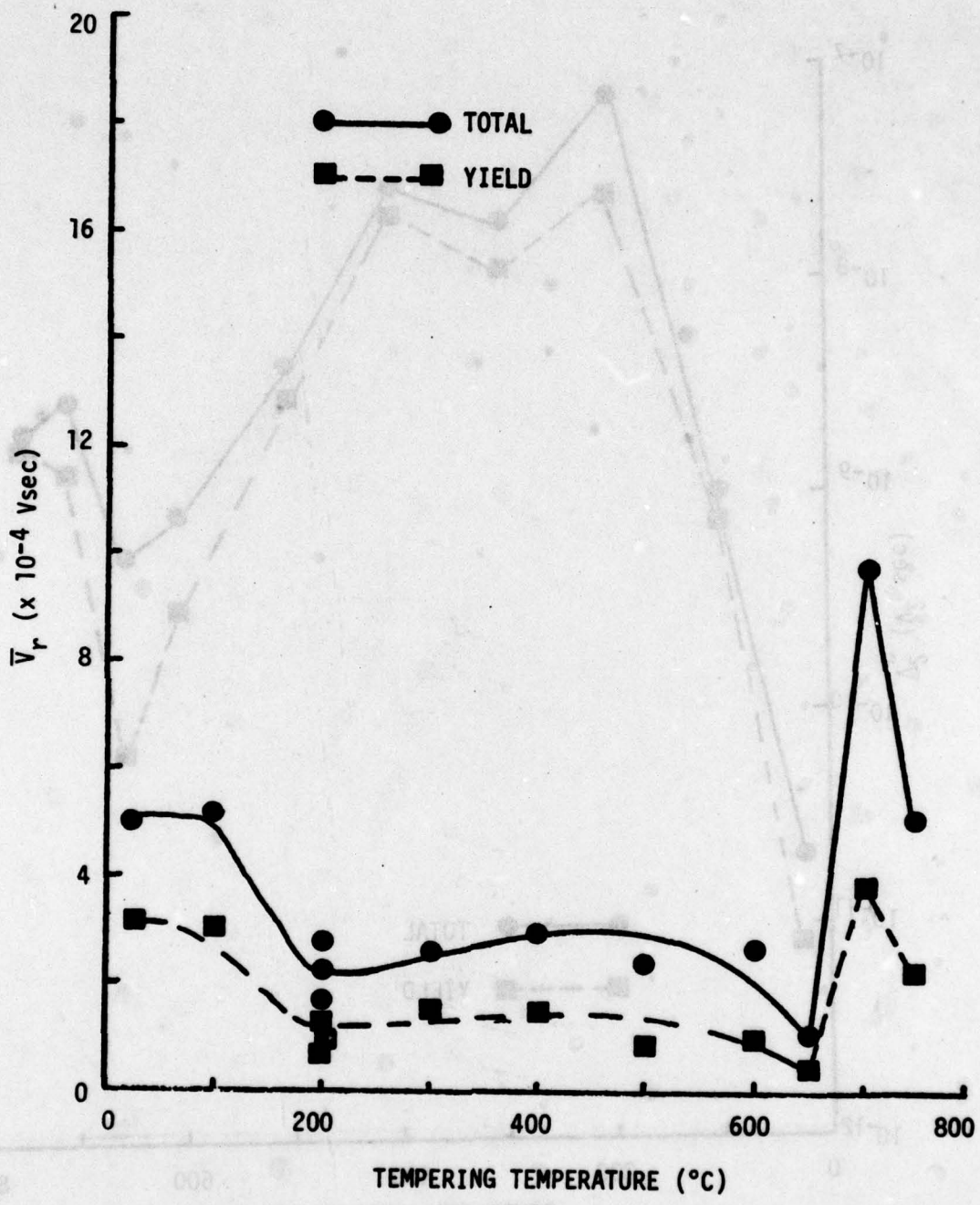

FIGURE 5.17 The integrated RMS level, $\bar{V}_r$, for bainitic steel as a function of tempering temperature.

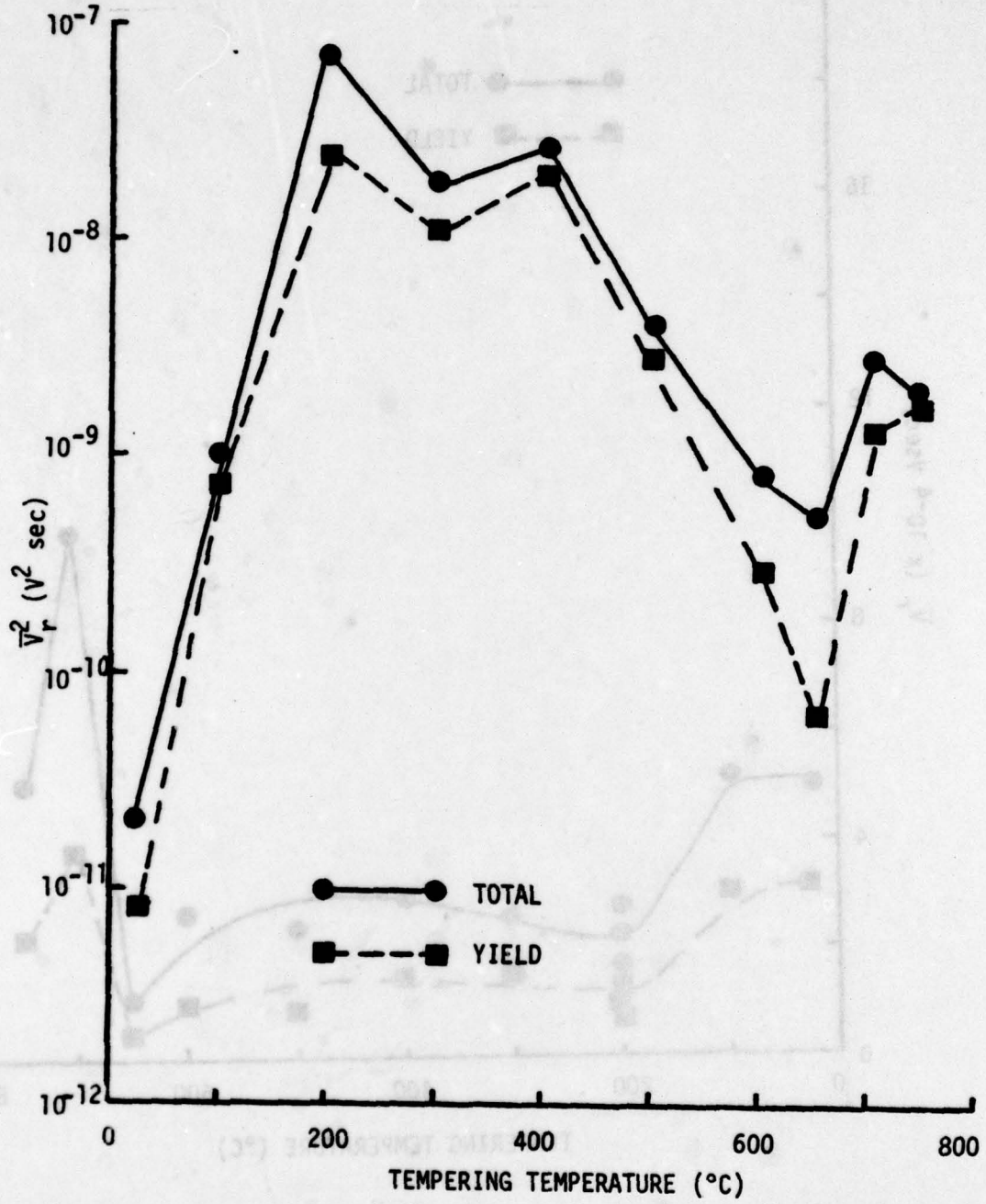

FIGURE 5.18 Integrated $\overline{V}_r^2$, against tempering temperature for quenched and tempered steel.

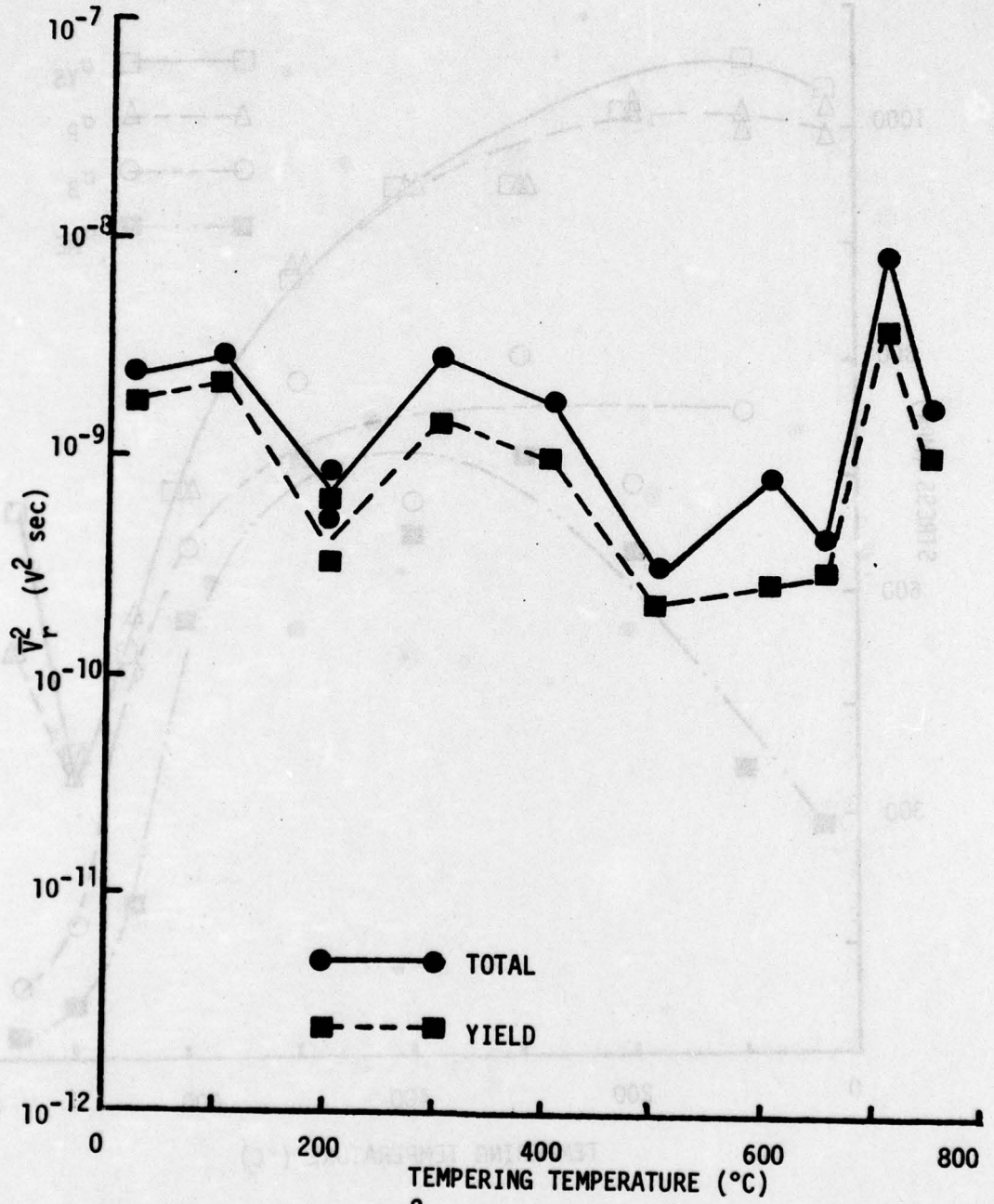

FIGURE 5.19 Integrated $\overline{V}_r^2$ against tempering temperature for normalized and tempered steel.

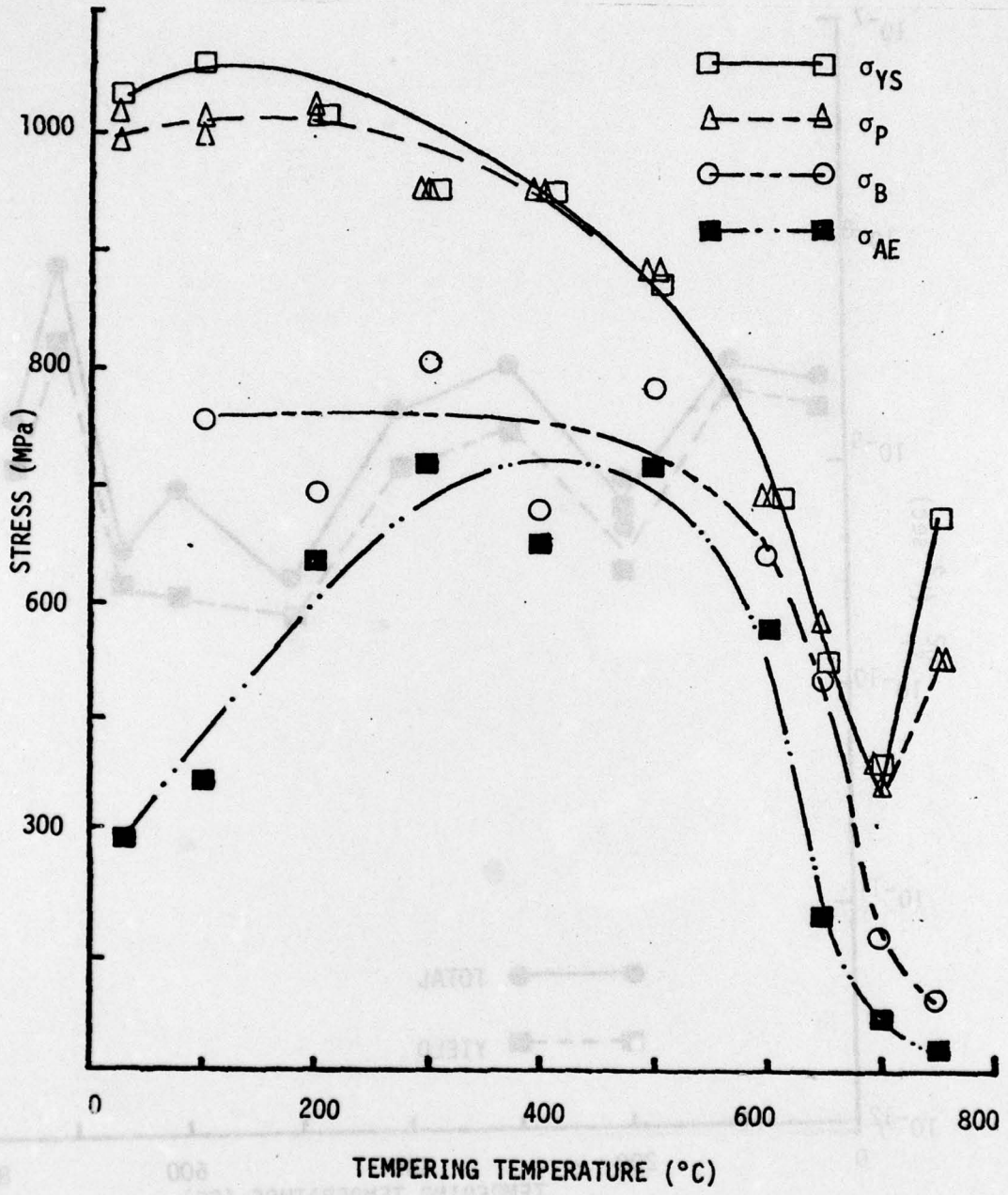

FIGURE 5.20 Stresses, σ_{YS}, σ_P, σ_{AE}, and σ_B against tempering temperature for martensitic steel.

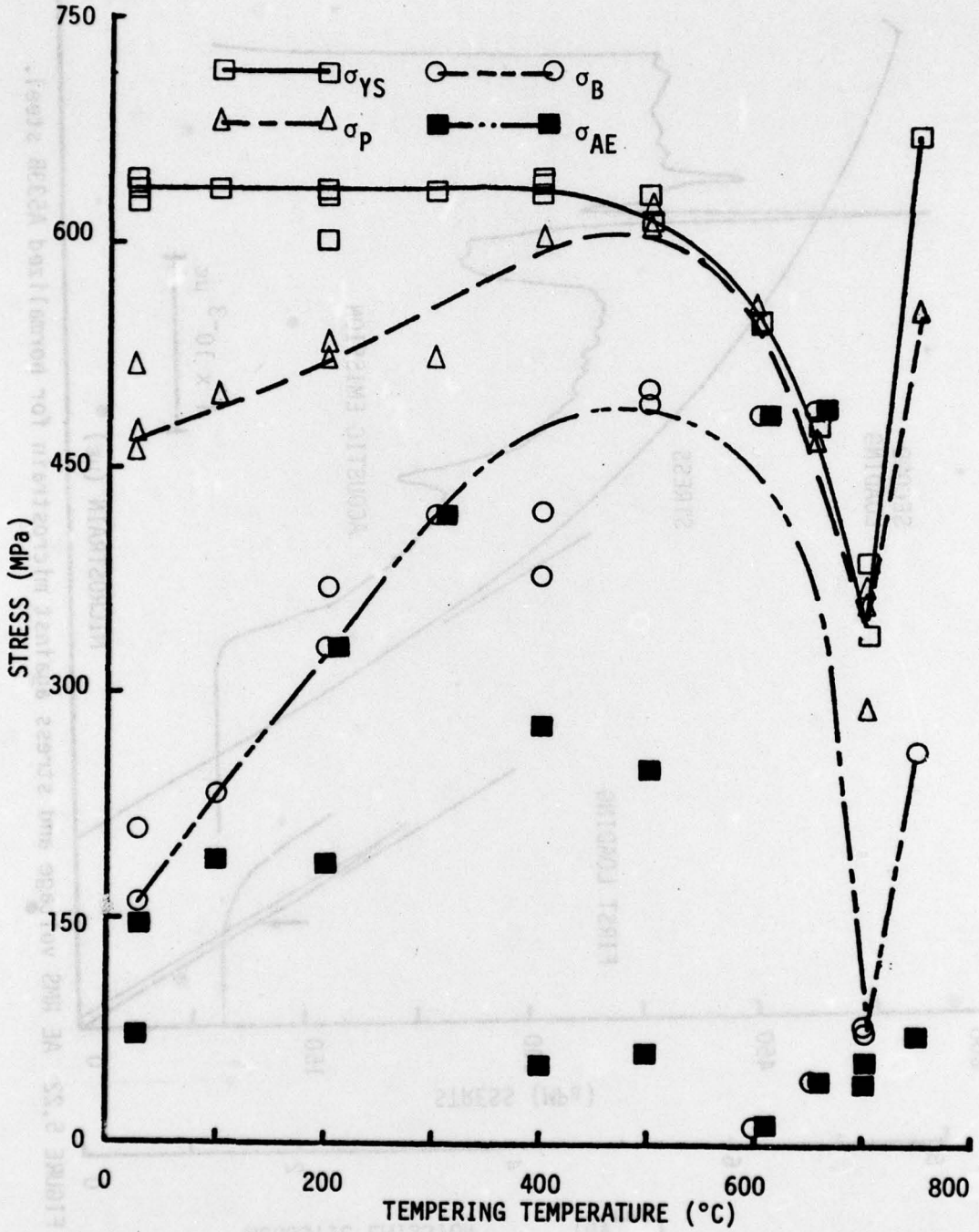

FIGURE 5.21 Stresses, σ_{YS}, σ_P, σ_{AE}, and σ_B against tempering temperature for bainitic steel.

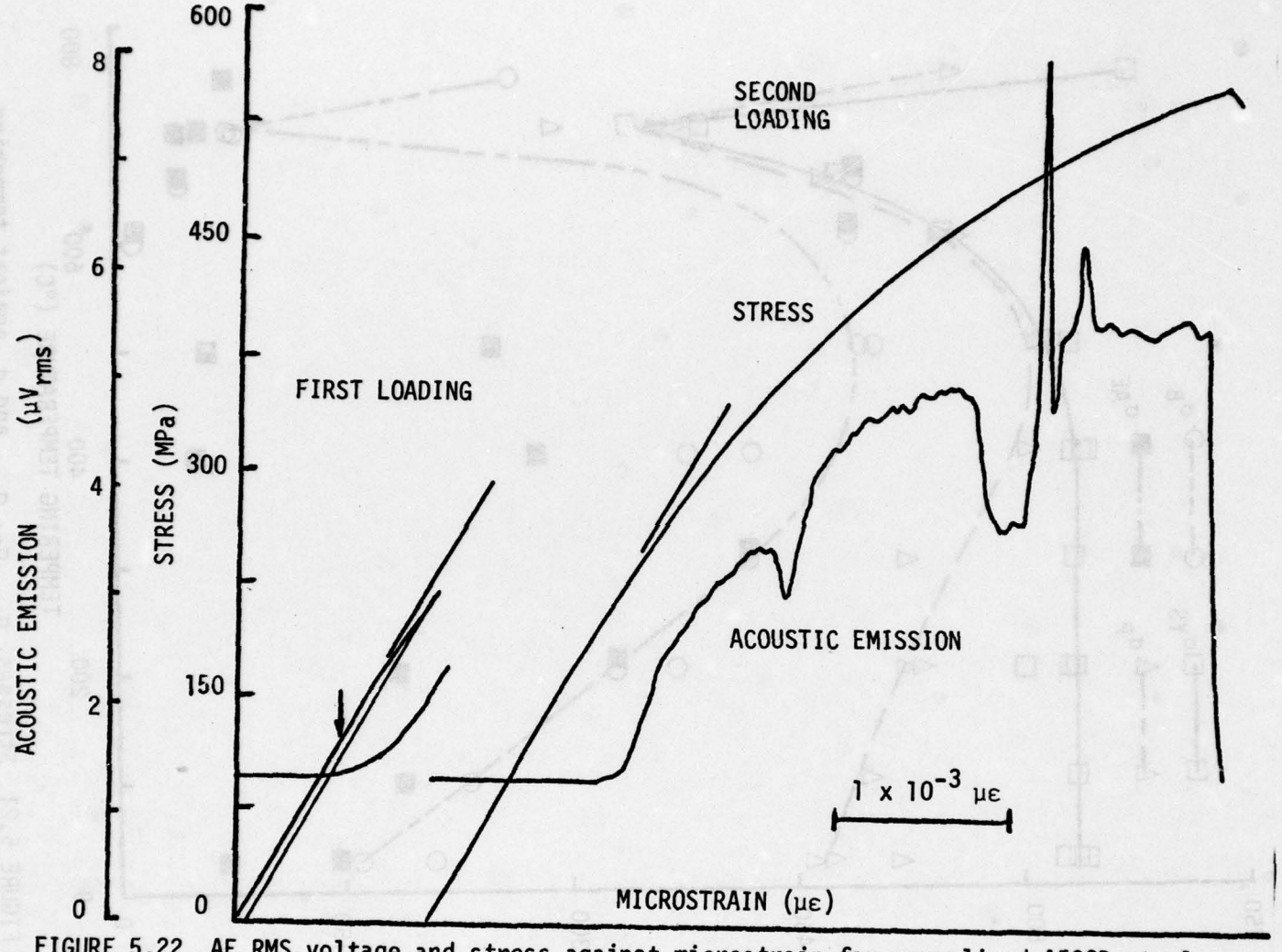

FIGURE 5.22 AE RMS voltage and stress against microstrain for normalized A533B steel.

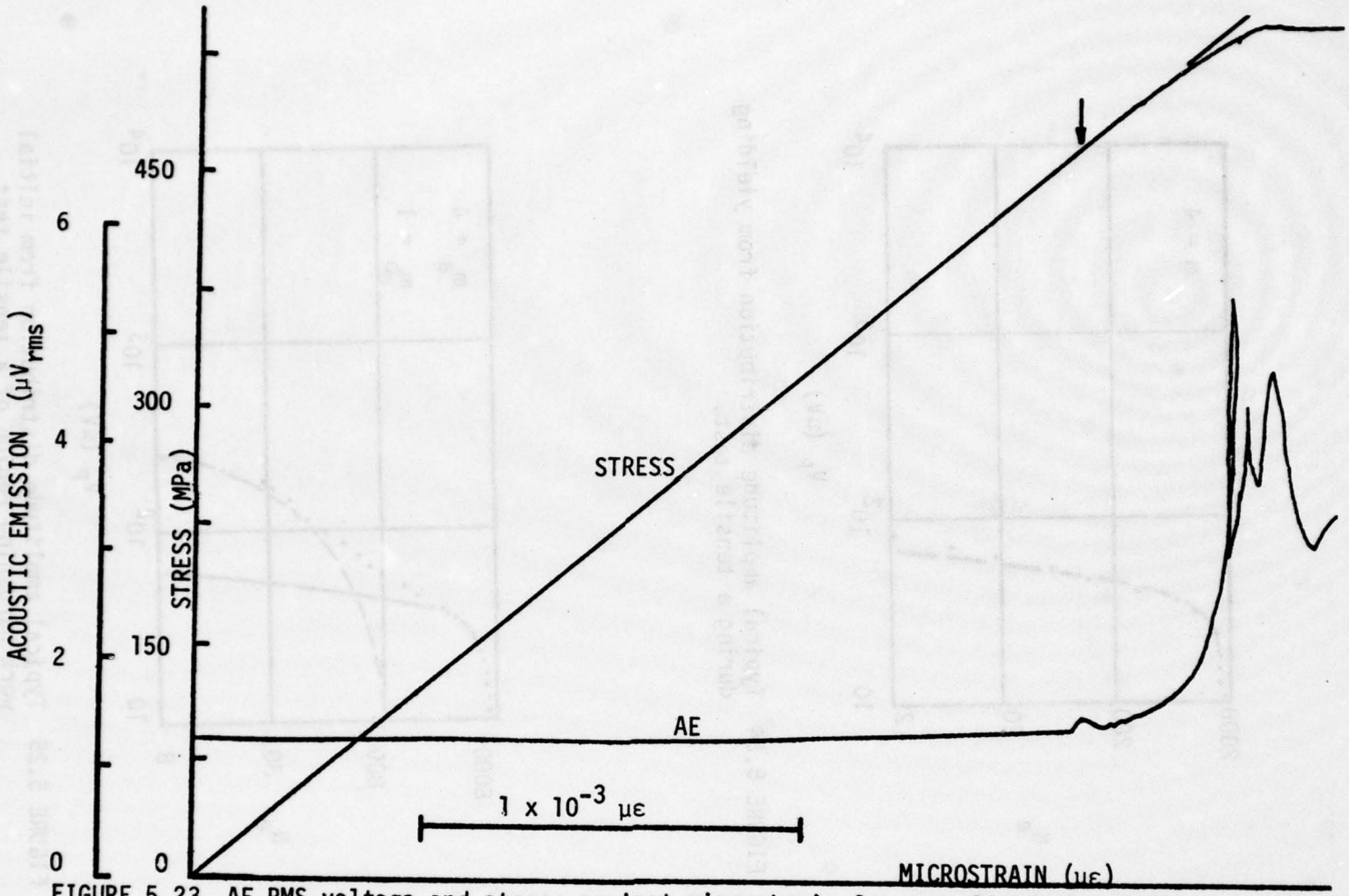

FIGURE 5.23 AE RMS voltage and stress against microstrain for normalized plus 600°C tempered A533B steel.

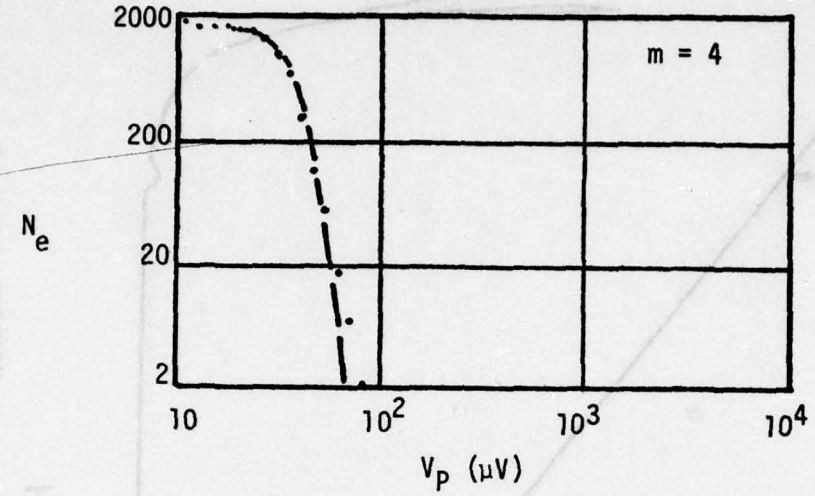

FIGURE 5.24 Typical amplitude distribution from yielding during a tensile test.

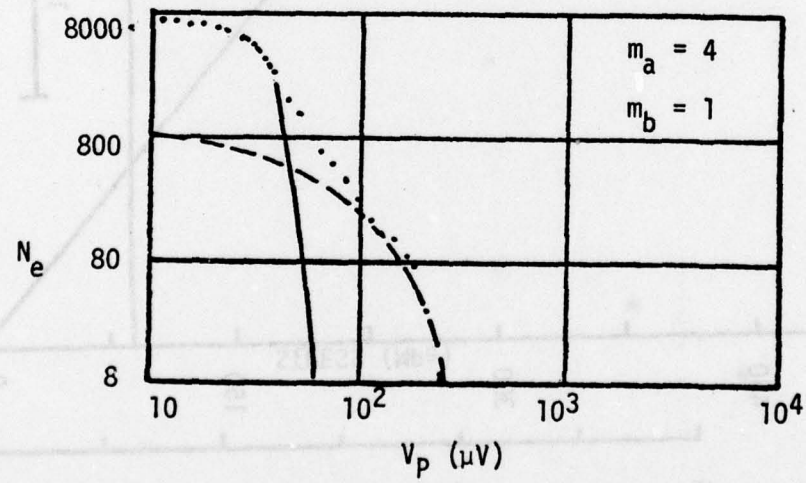

FIGURE 5.25 Typical amplitude distribution from initial work hardening region of a tensile test.

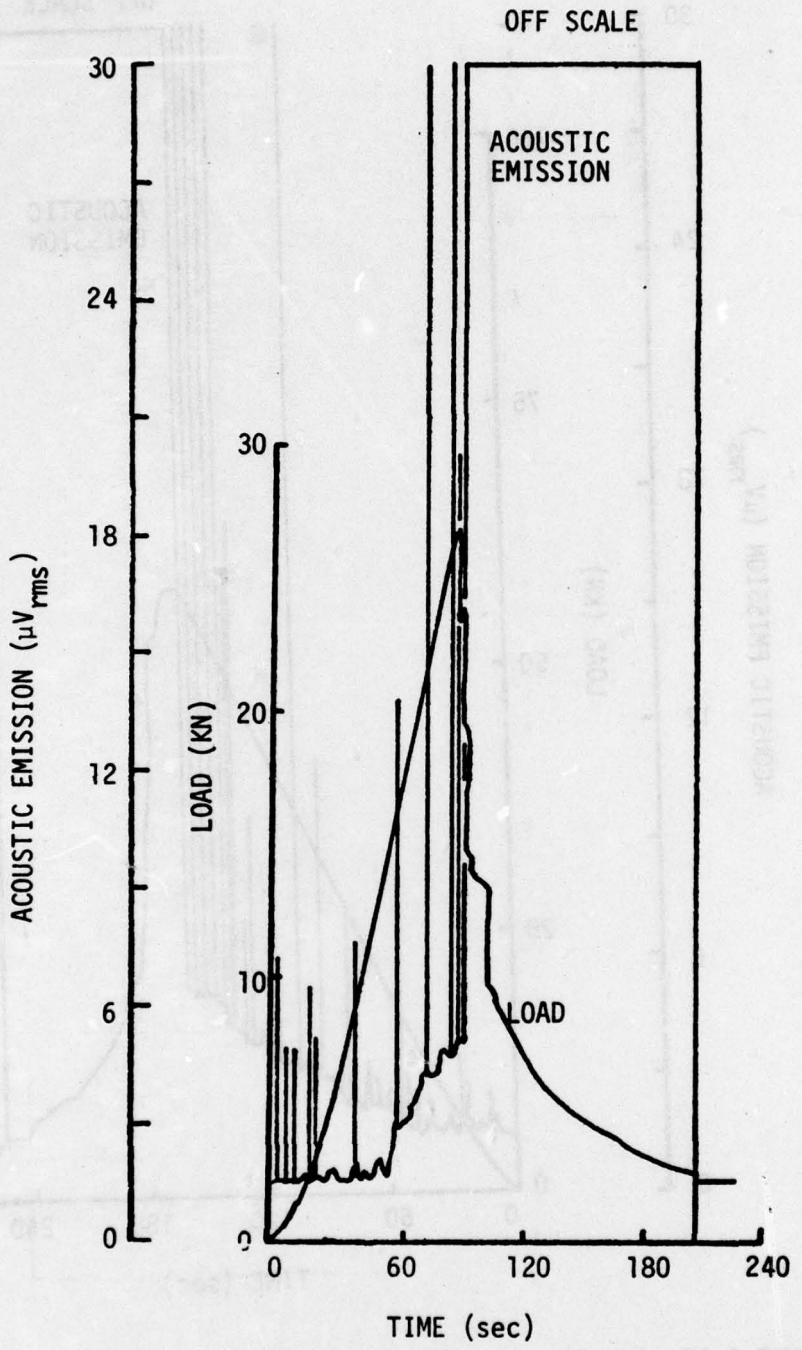

FIGURE 5.26 AE RMS voltage and load against time for the normalized compact tension sample.

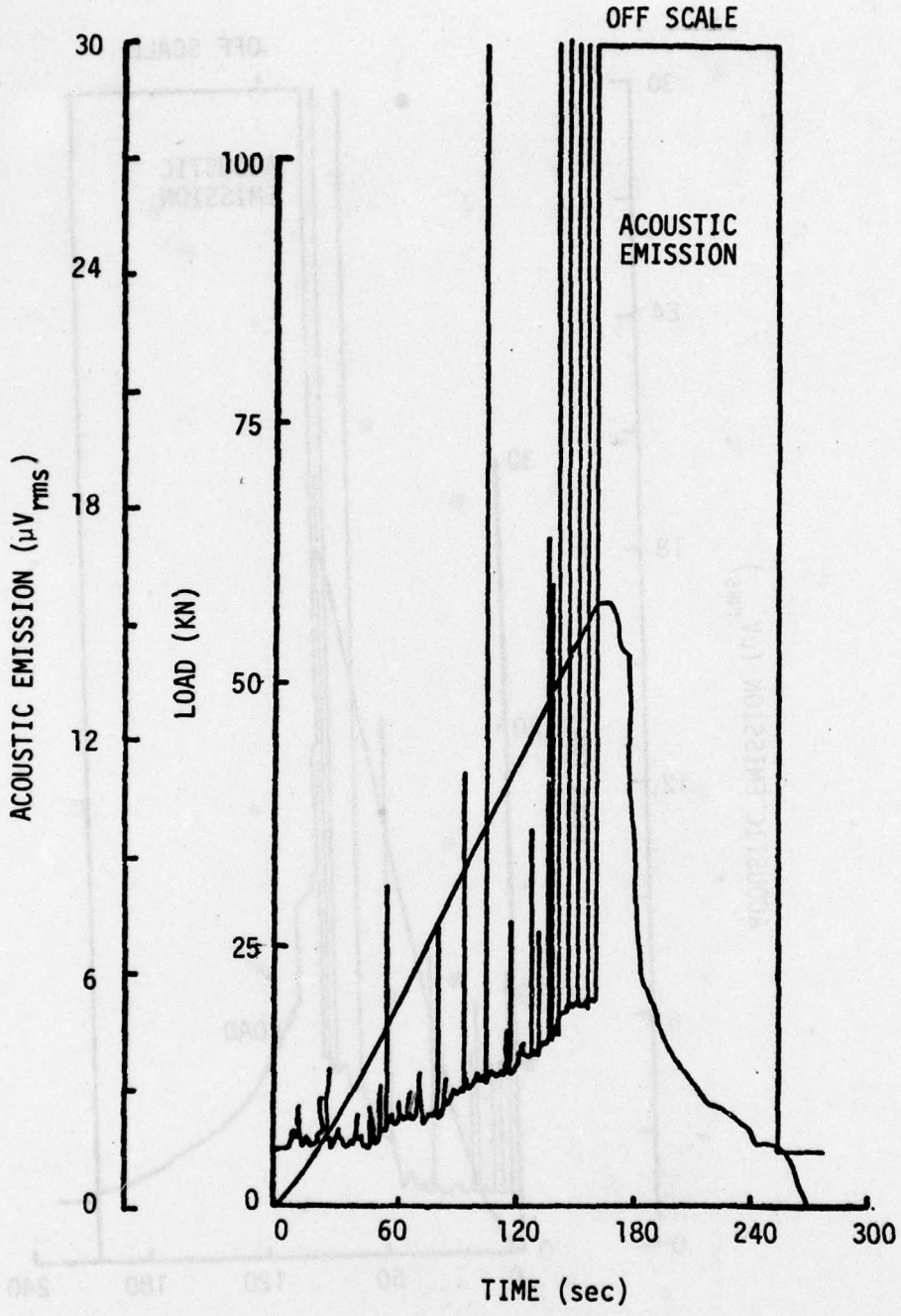

FIGURE 5.27 AE RMS voltage and load against time for the quenched plus 400°C tempered compact tension sample.

SEM

FIGURE 5.28 Fractograph showing cleavage in the full annealed condition tested at 25°C.

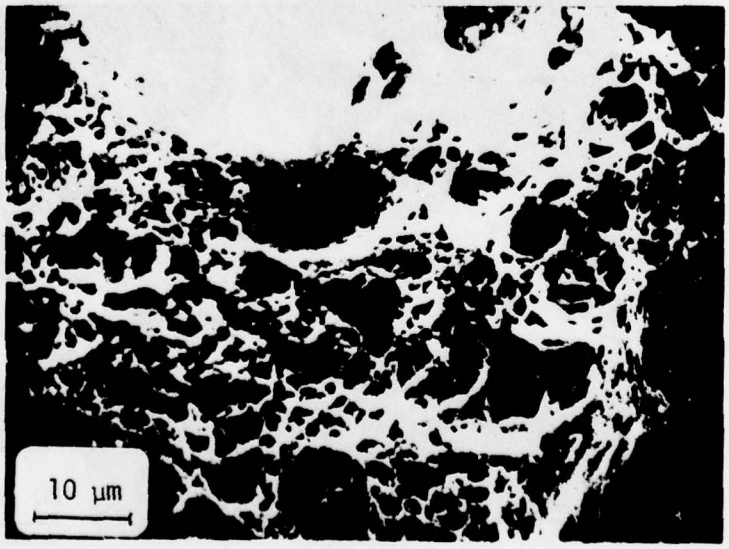

SEM

FIGURE 5.29 Fractograph showing dimple formation in the quenched plus 700°C tempered condition tested at 25°C.

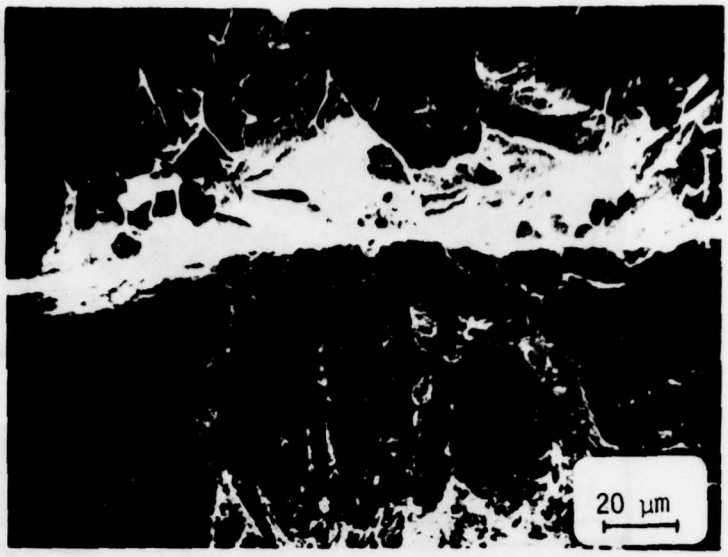

SEM

FIGURE 5.30 Fractograph showing the stretch zone formation in the as-received condition tested at 25°C.

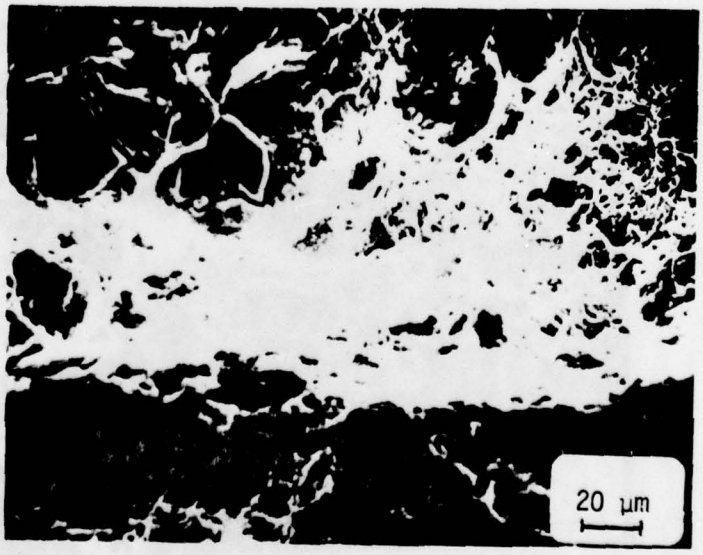

SEM

FIGURE 5.31 Fractograph showing the stretch zone formation in the normalized plus 400°C tempered condition.

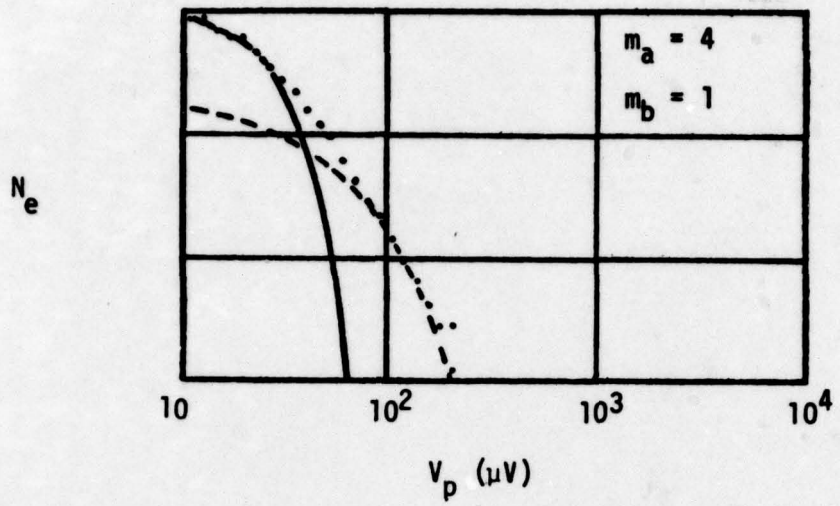

FIGURE 5.32 Typical amplitude distribution for loads up to P_Q.

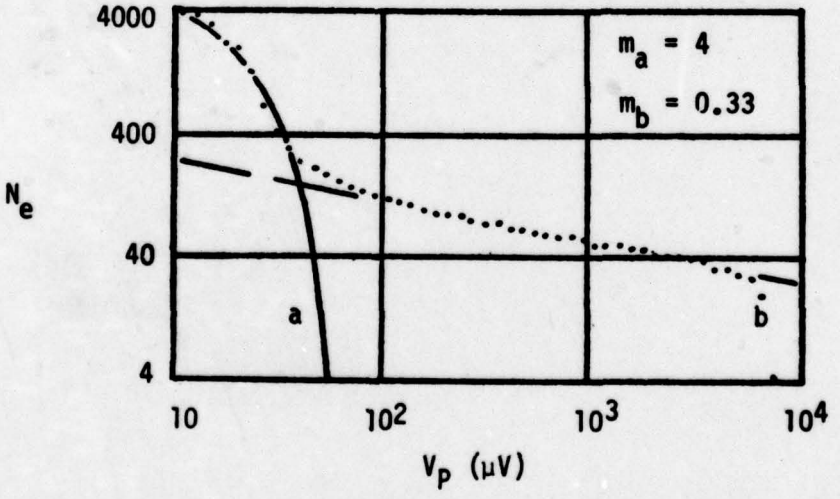

FIGURE 5.33 Typical amplitude distribution for loads above P_Q.